N95-13024

(NASA-CR-196432) WAVES IN SPACE
PLASMAS (WISP) Final Report (Iowa
Univ.) 42 p

Unclas

G3/75 0019722

NASA-CR-196432

FINAL
IN-75-CR
OCIT
19722
42P

FINAL REPORT
Waves in Space Plasmas (WISP)
Co-investigator Grant, NAG 5-1926

W. Calvert
Department of Physics and Astronomy
The University of Iowa
Iowa City, Iowa 52242

August 2, 1994

Activities under this project have included participation in the WISP program, a study of the data processing requirements for WISP, and theoretical studies of radio sounding, ducting, and magnetoionic theory.

WISP Participation

Throughout the project, virtually all of the WISP team meetings were attended and the project PI also participated in the WISP CDR and most other aspects the planning and design efforts of the program. This included writing functional objectives for various WISP measurement modes and otherwise assisting the program PI in the planning for WISP.

WISP Data System

Considerable time was spent planning a data system for WISP. This system would have provided personal computer and data-station access to the WISP data on CD ROM and been essential in the analysis of the complex data that WISP would have produced.

Sounder Theory

An analysis of radio sounding in the magnetosphere was prepared in conjunction a NASA study group headed by Dr. J. L. Green of GSFC and submitted to the NASA IMI Study Panel. One paper on this topic has been published, and a second manuscript on the theory and design of a magnetospheric radio sounder has been completed and is essentially ready for publication. This paper included a new theory of sounding for curved surfaces, an analysis of the effect of signal-to-noise ratio on sounder performance, and an analysis of the expected echoes from the magnetopause, plasmapause, and plasmasphere. Copies of these papers are attached.

Wave Ducting

Work on wave ducting was presented at the Kyoto General Assembly of URSI. This work included a comprehensive theory of ducting in different wave modes, and a manuscript on this topic remains in preparation.

Magnetoionic Theory

Although the formulation of magnetoionic theory by Stix has largely superseded that of Ratcliffe and Budden, the Appleton-Hartree Equation is often still cited as the dispersion relation of a magnetoplasma. The parameters, however, are different, and it wasn't clear how the Appleton-Hartree Equation should be expressed using the Stix parameters. The equivalent formula, in terms of the complex polarization ratio E_y/E_x, has been found to be as follows:

$$n^2 = \frac{PS - RL}{P - S} - \frac{(PS - RL)/(P - S) - P}{1 - i\,(E_y/E_x)\,[\,(P - S)/D\,]\cos\theta}$$

where

$$i\,\frac{E_y}{E_x} = \frac{(PS - RL)\sin^2\theta}{2\,P\,D\cos\theta} \pm \sqrt{\frac{(PS - RL)^2\sin^4\theta}{4\,P^2 D^2\cos^2\theta} + 1}$$

The usual formula results from substituting the latter into the former, and unlike the original Appleton-Hartree formula, this formula is applicable to all wave modes. This result new will be useful in future analyses of wave propagation.

REMOTE SENSING OF SUBSTORM DYNAMICS VIA RADIO SOUNDING

P. H. Reiff, J. L. Green, R. F. Benson, D. L. Carpenter, W. Calvert, S. F. Fung, D. L. Gallagher, Y. Omura, B. W. Reinisch, M. F. Smith and W. W. L. Taylor

ABSTRACT

This paper describes the technique of magnetospheric radio sounding and shows how it can be applied to produce "images" of magnetospheric electron density distributions and their variations during substorms. The magnetospheric radio sounder is based on more than a half-century heritage of ionospheric sounding combined with modern digital techniques. Coded pulses are transmitted by a long dipole and the delay times and directions-of-arrival of the returning pulses are measured. Plasma densities from 0.1 to 10^5 cm^{-3} can be remotely sensed simultaneously along several different directions by a digital sounder operating in the 3 kHz to 3 MHz range. Positions of magnetospheric plasma and magnetic boundaries, such as the plasmapause and magnetopause, can be monitored on a time scale of a few minutes, and plasmaspheric erosion and refilling quantified during a substorm cycle. Such measurements have previously been impossible to obtain. From a sounder suitably situated in the near-earth tail lobe, one can measure the magnetotail cross-section and get information on the field strength, thus allowing monitoring of total tail flux changes during a substorm and thus the difference between dayside and nightside merging rates. It may also be possible to sound a near-Earth plasmoid directly and thus sense its position, growth, and motion.

INTRODUCTION

The Earth's magnetosphere is extremely dynamic, with large-scale changes in size and shape in response to interplanetary conditions, and major internal reconfigurations in response to substorms. Single-spacecraft measurements allow determination of magnetospheric conditions only at specific points at any given time. Remote sensing techniques, such as auroral imaging, can aid our understanding tremendously by allowing monitoring of the footprint of some of the plasma domains. Auroral images, however, reflect only precipitating particles; particles trapped in the equatorial plane or those in the magnetospheric boundary layers typically do not precipitate at all. Remote sensing by means of far ultraviolet (FUV), extreme ultraviolet (EUV), X-ray, and energetic neutral atom (ENA) detection promises a great step forward in monitoring magnetospheric domains [*Williams et al.,* 1992].

During the NASA Space Physics Strategy-Implementation Study of 1990, we suggested using radio sounders to study the magnetopause and its boundary layers [*Reiff,* 1991], and to study the plasmasphere [*Green and Fung*, 1994]. The magnetopause, plasmasphere, as well as the cusp and boundary layers, can be remotely monitored if a radio sounder is placed on a high-inclination polar-orbiting spacecraft with a reasonable (≥6 R_E) apogee (Figure 1, from *Reiff et al.* [1994]).

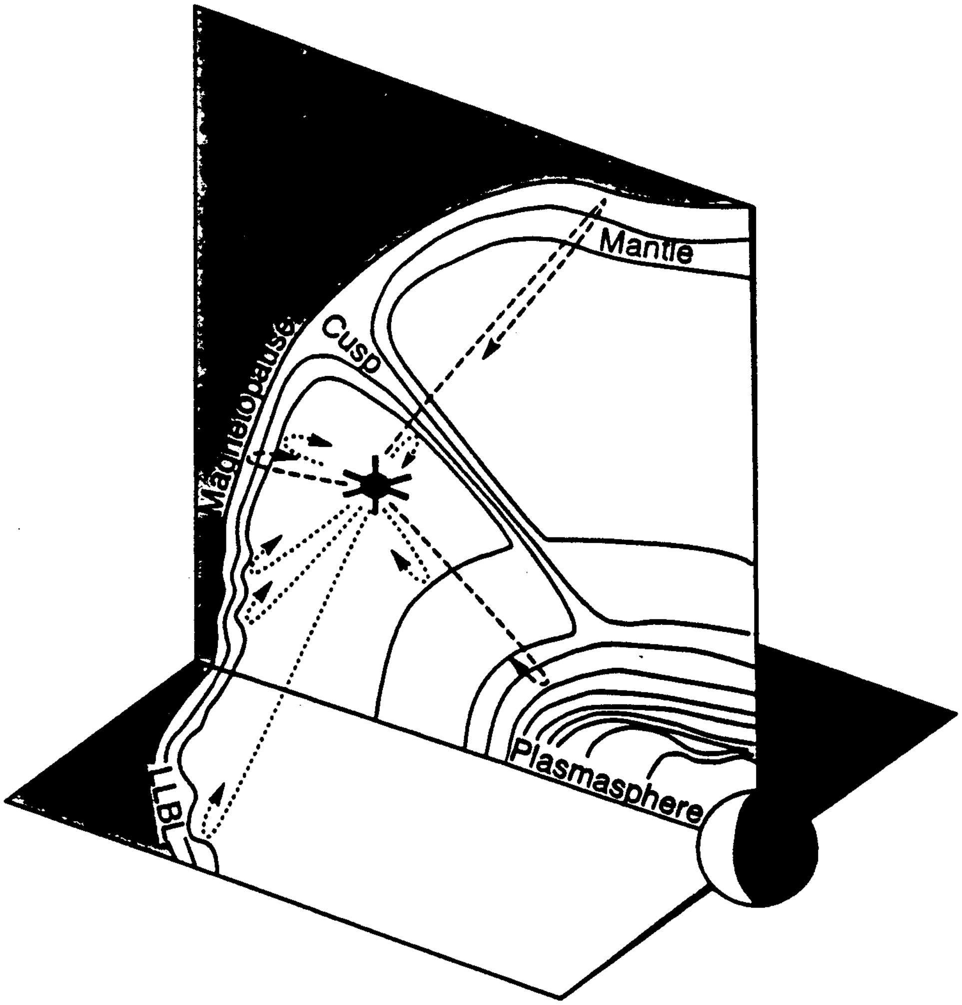

Figure 1. Schematic contours of constant plasma density in the sunward side of the magnetosphere. A radio sounder on a polar-orbiting spacecraft can remotely sense the density structures at the magnetopause, the plasmapause, the auroral density cavity and the magnetospheric cusp, thus creating quantitative "images". Lower-frequency waves (dotted) probe the low-density surfaces, while higher-frequency waves (dashed) probe the higher-density structures. Waves on the boundaries yield multiple reflecting points, allowing a crude image within a few minutes and a composite image as illustrated within the time required for a quarter of a spacecraft orbit, by combining successive electron density profiles along the orbit [from *Reiff et al.*, 1994].

Radio sounding techniques date back to the study of the ionosphere by *Breit and Tuve* [1926]. Swept-frequency ground-based sounders are used to monitor the electron number density (N_e) structure of the ionosphere up to the F-layer density peak with high time resolution. The early instruments evolved into a global network which produced high-resolution ionograms (displays of echo delay versus frequency) on 35 mm film. The bottomside electron density profiles deduced from these records provided one of the cornerstones of the success of the International Geophysical Year [*Berkner*, 1959].

Topside ionospheric densities, above the F-layer density maximum, were first measured in the Alouette/ISIS (International Satellites for Ionospheric Studies) program [*Franklin and Maclean*, 1969; *Jackson et al.*, 1980]. A series of consecutive profiles can be combined to create orbital-plane N_e contours from the satellite altitude to the altitude of the F layer peak density [*Nelms and Lockwood*, 1966 and *Benson*, 1985 and references therein]. Comparisons of densities from topside and bottomside sounders, and multi-spacecraft studies have indicated that the error of the Alouette/ISIS-derived N_e values is typically within 10%, even at the most remote distances [*Whitteker et al.*, 1976; *Hoegy and Benson*, 1988 and references therein]. ISIS demonstrated the synergism between sounders and optical imagers on the same spacecraft [*Lui and Anger*, 1973; *Shepherd et al.*, 1976]. Digital technology was used in later spacecraft sounders, such as in Japan's ISS-b (Ionosphere Sounding Satellite), Ohzora (also called EXOS-C), and Akebono (or EXOS-D) spacecraft; and in the USSR's Intercosmos 19 and Cosmos 1809 missions [see *Green et al.* 1994 and references therein]. ISIS also showed the ability to remotely sound the magnetospheric cusp [Dyson and Winningham, 1974]. The ISIS-C spacecraft would have contained a sounder with a similar orbit and similar science objectives to that discussed here, but was never flown [J. D. Winningham, personal communication, 1994].

Bottomside (ground-based) ionospheric sounders have enjoyed great advances over the last few decades [*Hunsucker*, 1991]. These advanced ionospheric sounders can measure the frequency, time delay, amplitude, phase, Doppler shift and spread, polarization, and direction of arrival of the echo. Two sounders in this class are the Dynasonde (developed at the U.S. Department of Commerce Laboratories in Boulder) and the Digisonde (developed at the University of Massachusetts Lowell). These instruments offer a high degree of flexibility in measurement format since their operations are controlled by software [*Reinisch*, 1986]. Evidence that their scientific capabilities go far beyond the N_e profiles of the standard ionosondes is indicated from results that show, for example, turbulence, drifts, winds and structures [*Wright and Hunsucker*, 1983; *Buchau et al.*, 1988]. A new generation of spaceborne sounders can use these latest techniques [*Reinisch et al.*, 1992] to make sounding of the magnetosphere possible with very modest power requirements by taking advantage of spread spectrum pulse compression and Fourier transform processing. A 500m tip-to-tip dipole is planned as transmitting antenna.

RADIO WAVE SOUNDING OF THE MAGNETOSPHERE

Radio wave sounding of the magnetosphere uses the same fundamental principles as ionospheric sounding. A cold magnetized plasma supports two freely propagating electromagnetic waves, the O (ordinary) and X (extraordinary) modes, each with distinct phase velocity and polarization [*e.g.*, *Chen*, 1974]. The propagation characteristics of these waves are determined by the local electron plasma frequency, f_p , and electron gyrofrequency, f_g.

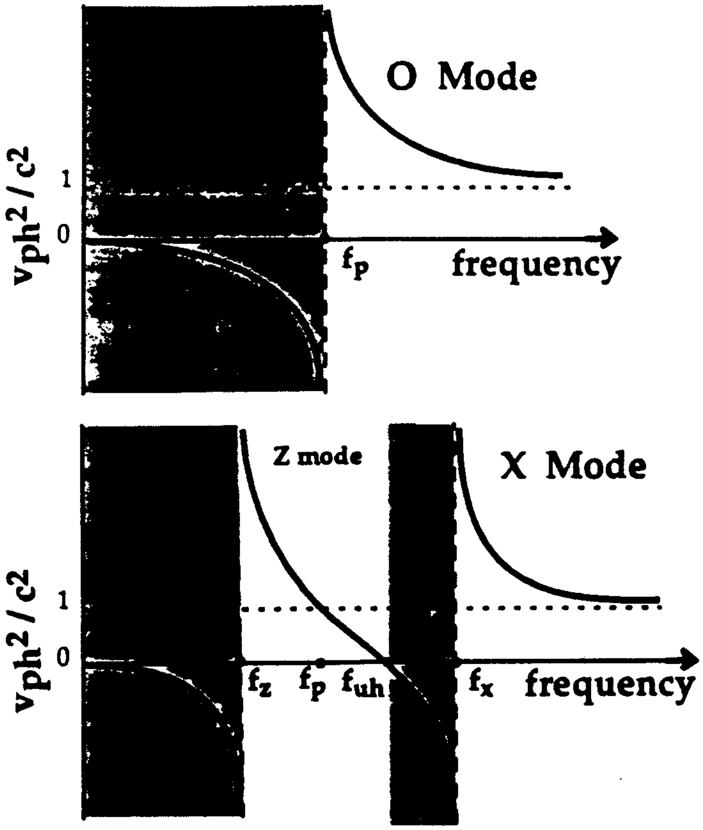

Figure 2. A schematic phase velocity -frequency diagram showing the ordinary (O Mode) and extraordinary (X Mode) propagation modes supported by a cold plasma. (The shaded areas indicate regions of non-propagation). The extraordinary mode has two branches. The lower frequency branch (often called the Z mode) is trapped between a lower frequency cutoff f_z and an upper resonant frequency varying between f_p and f_{uh}, depending on the angle of propagation [*Ratcliffe*, 1959]. The high frequency branch is normally referred to as the X mode. For the purposes of remote sensing, the O and X modes are used because they propagate at all frequencies above their cutoffs at f_p and f_x, respectively. From a knowledge of the plasma frequency, the electron density can be derived; from the f_x frequency, the gyrofrequency (and thus the field strength) can be derived. [Adapted from *Chen*, 1974.]

Figure 2 shows the variation of the square of the ratio of the wave phase velocity v_{ph} to the speed of light c on a scale of increasing frequency, for several wave modes. The cross-hatched regions represent the forbidden frequency ranges in which the indicated waves cannot propagate. The Z mode has a lower frequency cutoff f_Z (when $v_{ph}^2/c^2 = \infty$) and an upper frequency resonance (when $v_{ph}^2/c^2 = 0$) that restricts its propagation and is thus referred to as a trapped mode of the plasma. This wave mode is unsuitable for use in direct sounding to great distances. The whistler mode (not shown in the figure) is also a trapped mode.

Since the X and O modes have no propagation restrictions above their low frequency cutoffs (Figure 2), they are suitable for remote radio sounding. The cutoff for the O mode is the local plasma frequency f_p,

$$f_p = \frac{1}{2\pi}\sqrt{\frac{N_e e^2}{\varepsilon_0 m}} \approx 9\sqrt{N_e}\ kHz \tag{1}$$

when N_e is expressed in cm^{-3}; ε_0 is the permittivity of free space, e is the electron charge and m is the electron mass. For the X mode, the cutoff f_X is

$$f_x = \sqrt{f_p^2 + \frac{1}{4} f_g^2} + \frac{1}{2} f_g \quad (2)$$

where $$f_g = (1/2\pi)eB/m = 28.0 \text{ B (Hz)} \quad (3)$$

when B, the magnetic field strength, is expressed in nT. These two modes propagate freely with group velocity $v_g \approx v_{ph} \approx c$ when the wave frequencies are well beyond the plasma cutoffs; thus they are called the free-space modes.

A swept-frequency sounder transmits and receives a sequence of X and O mode pulses, with the frequencies increasing stepwise. When the transmitted waves enter a region of increasing plasma density or magnetic field strength, the pulse is reflected when the wave frequency matches the cutoff frequency. Most of the inner magnetosphere has a relatively low density – thus a satellite lies between increasing density gradients at the magnetopause and at the plasmasphere (see Figure 1). For most magnetospheric applications the primary echo paths will be approximately perpendicular to the plasma density contours at reflection. A data record (plasmagram) consists of the time delay and amplitude, along with complex Doppler and angle-of-arrival information, for each sounding frequency and polarization.

Thus the swept-frequency measurements permit the determination of the electron plasma density profiles of remote plasma regions [see, *e.g.*, *Jackson et al.*, 1980; *Huang and Reinisch*, 1982], so long as the density is generally increasing with distance. Magnetospheric density structures are quite dynamic in space and in time. Thus each transmission will typically result in more than one echo (Figure 3). Returns will usually be obtained from several directions for the same frequency transmission, but each will exhibit a different time delay, angle of return, and Doppler shift, thereby allowing a rough cross-section within minutes. From a sequence of profiles taken during a portion of a single orbit, one can produce two-dimensional, cross-sectional magnetospheric images (Figure 1). Raytracing studies indicate that from a dayside position much as in Figure 1, signal returns would also be received from the dawn and dusk magnetopause [*Fung et al.*, 1994]. Thus information on the 3-D magnetospheric N_e structures will also be obtained. For more information on the technique and applications of magnetospheric radio sounding, see *Green et al.*, 1993; *Reiff et al.* [1994], *Fung et al.*[1994], *Green et al.*[1994], and *Calvert et al.* [1994].

THE USE OF SOUNDING IN SUBSTORM STUDIES

A radio sounder is ideal for studying the global structure and dynamics of the plasmasphere and its outer boundary, the plasmapause. The plasmasphere reacts sensitively to changes in magnetospheric convection, with the plasmapause varying in geocentric distance between 2 and 7 R_E as magnetospheric conditions change from active to quiet [*Carpenter*, 1966; *Spiro et al.*, 1981].

A radio sounderis ideally suited to study such dynamic changes since it can provide a sequence of nearly instantaneous plasmaspheric electron density profiles. Therefore, nearly the same region can be probed repeatedly within minutes, allowing us to separate spatial from temporal variations. Thus a sounder can provide, for the first time, observations of the formation of a plasmapause boundary at a new location during substorms, and of plasmatrough refilling beyond a newly formed plasmapause. Under certain viewing conditions, the distribution and movements of dense plasmas being eroded from the main plasmasphere during substorms can be observed, thus permitting the study of the development of outlying "detached" or "connected" cold plasma regions. The possible decoupling of the high altitude and low altitude convection regimes can also be investigated [e.g. *Carpenter et al.*, 1993]

A sounder, by monitoring the location of the magnetopause and the time evolution of the magnetopause boundary layers, can determine (1) the variability of plasma mantle density and thickness in response to the southward and westward components of the IMF, and (2) the passage of wave structures in the low-latitude boundary layer [*Rosenbauer et al.*, 1975; *Paschmann et al.*, 1978; *Paschmann*, 1984]. One can readily determine from a sequence of sounder measurements whether the inner edge of the boundary layer moves only in phase with the magnetopause motion (Figure 3, left), or whether the thickness of the layer varies in time as the plasmas move downstream (Figure 3, right [from *Reiff et al.*, 1994]).

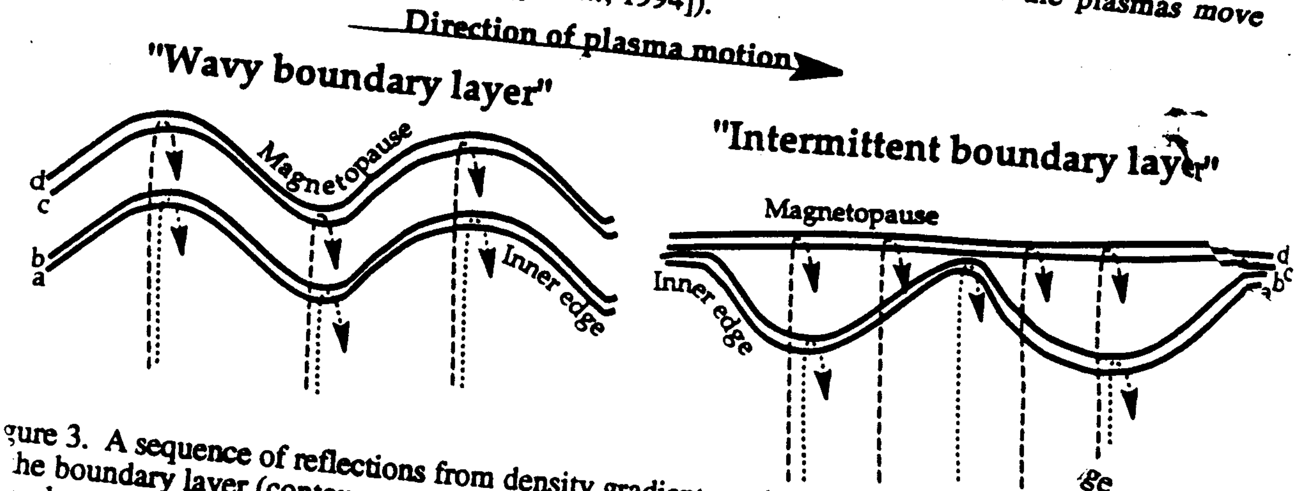

gure 3. A sequence of reflections from density gradients at the magnetopause and
he boundary layer (contours are labeled *a, b, c* and *d* in increasing density).
ve know that the boundary layer has a relatively sharp density gradient at the
arp gradient at the inner edge, with a "ledge" in between [*Sckopke et*
0], and that these boundaries are constantly in motion. It is not
kness of the boundary layer is nearly constant (left) or variable
dings at low (dotted) and high (dashed) frequencies as the struc
question should be resolved [from *Reiff et al.*, 1994].

ge
and
al.,
if the
ssive
ecraft,
determin
ltaneous
d data fr
94
Page

radio sounder, by using its direction-finding capability
stance from the spacecraft to one or more location
et al., 1994]. By comparing sounder observatio

solar wind monitoring spacecraft such as WIND and IMP-8, one can test the solar wind dependence of empirical magnetopause models such as *Sibeck et al.* [1991], *Roelof and Sibeck* [1993], and *Petrinec and Russell* [*1993a, b*].

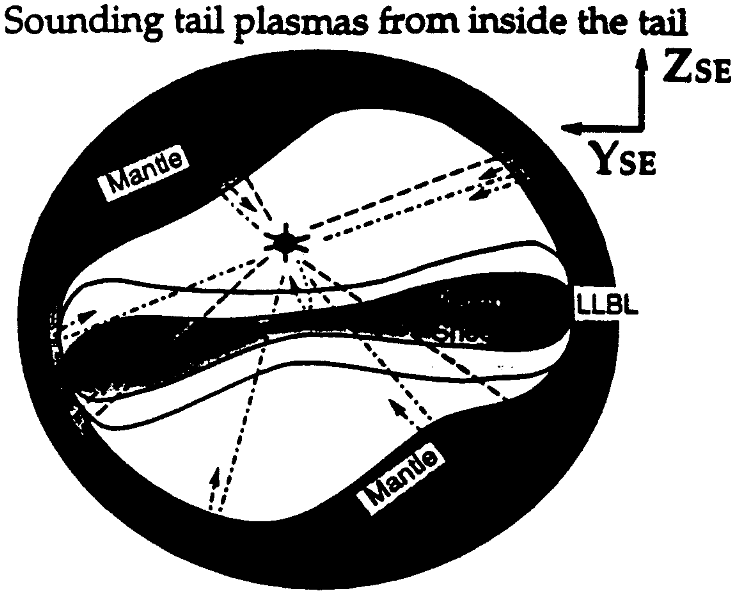

Figure 4. A schematic of reflections from density gradients at the magnetopause and its boundary layers from a spacecraft (or a lunar base) within the cislunar magnetotail lobe. The concave density cavity provides an enhancement of the return signal and allows multiple returns from a single transmission, yielding a multipoint tail cross-section on less than minute time scales. The plasma sheet is of such low density that middle- (dash-dot) and high-frequency signals (dashed) can sound right through to reach the far boundary layer and magnetopause, or a low-frequency signal (dotted) can probe the near edge of the plasmasheet from the lobe. (Beyond lunar distance, most of the lobe is full of plasma and the density contrast at the plasma sheet is insufficient for a signal return, but the magnetopause should still yield a detectable signal).

In the special case of spacecraft near apogee in the near-Earth magnetotail (or a lunar-based instrument when the Moon is in the magnetotail [*Reiff*, 1991; *Green and Fung*, 1994]), one can receive the reflected signals from both the dawn and duskside equatorial magnetopause and north and south high latitude magnetopause nearly simultaneously (Figure 4). It can then determine whether the magnetospheric tail is flattened and/or twisted by the IMF, as has been proposed [*e.g. Fairfield*, 1992 and references therein]. By determining the size of the magnetotail and having some information about the field strength derived from the X mode echoes, it will be possible to monitor the magnetic flux in the magnetotail and thus the net (dayside minus tail) magnetic merging rates [*Russell and McPherron*, 1973]. Note that a sounder system located in the high-latitude lobes may be able to sound through the low-density plasmasheet to the far side magnetopause.

In certain geometries, it may also be possible to monitor the growth and motion of plasmoids in the magnetotail. In the near-earth neutral line model of a substorm [*Hones*, 1979], a plasmoid forms, grows, and disconnects in a substorm cycle [e.g. *Baker et al.*, 1987; *Slavin et al.*, 1989]. If a sounder is situated in the high-latitude lobes (*e.g.*, at $X_{SM} \sim -20\ R_E$, $|Z_{SM}| \sim 10$), it may be able to sound off the density enhancement of the growing and moving plasmoid. A schematic of this reflection geometry is shown in Figure 5 (adapted from *Richardson and Cowley*, 1987]. In the near-earth magnetotail ($<100\ R_E$), the magnetotail lobe density is much smaller than the plasmasheet density [*Slavin et al.*, 1985] and a sounder should be able to remotely sense a plasmoid. In the distant (>100 R_E) magnetotail, however, the lobes have a great deal of plasma in them and the density contrast is not sufficient to return an echo from the plasmoid [Frank and Paterson, this volume].

A plasmoid moving down tail past the sounder may allow a sequence of soundings to yield information on the growth and motion of the plasmoid, and monitoring of the deformation of the magnetopause as the plasmoid moves [e.g. *Slavin et al.*, 1993]. A schematic of the possible geometry is shown in Figure 6. As a first test of this idea, we have taken the MHD plasmoid model developed by *Omura and Green* [1993] and performed raytracing calculations with a test sounder in the near-Earth magnetotail lobe. A set of sample rays emanating from the spacecraft are shown bouncing off of the plasmoid (Figure 7). Here the sounding frequency is near 11 kHz, corresponding to a density of about 1.5 cm^{-3}. Divergence of the rays as they refract off the plasmoid indicate the defocusing aspect of the convex surface [*Reiff et al.*, 1994; *Calvert et al.*, 1994].

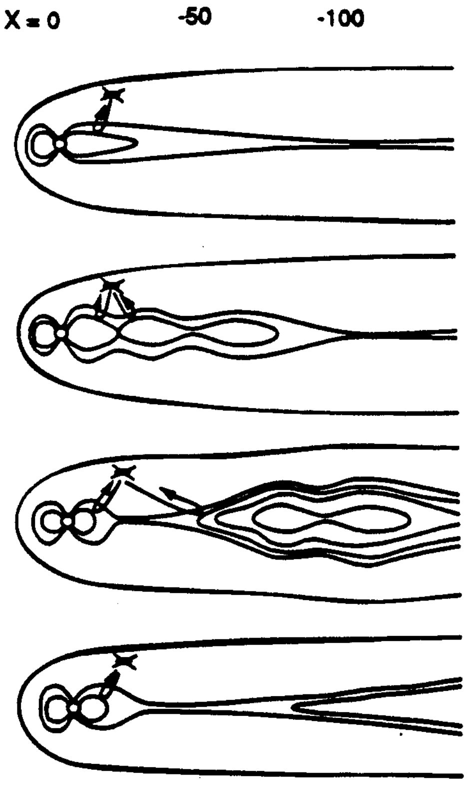

Figure 5. A schematic of reflections c sounder rays (dashed) from density gradient associated with plasmoids. A sounde situated in the low-density magnetotail lob may be able to monitor the growth and motio of a plasmoid during the substorm cycl [adapted from *Richardson and Cowle* 1987].

Sounding Plasmoids

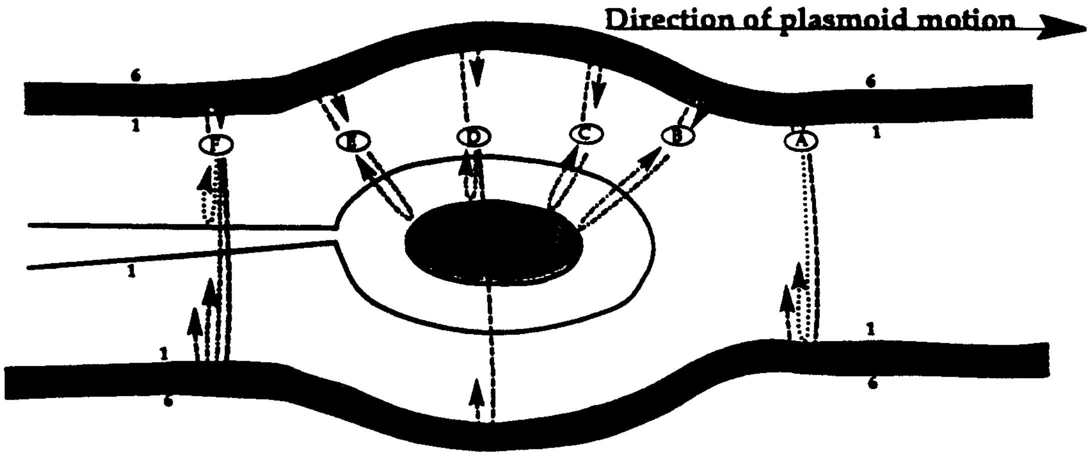

Figure 6. Schematic of sounding off a plasmoid from a cislunar magnetotail location as the plasmoid moves downtail. A sounder will effectively move from locations A, to B, C, etc. The highest frequency transmissions (shown dashed) pass through the plasmoid and/or the plasma sheet and reflect from the magnetopause; middle frequencies (dash-dot) sense the plasmoid or the

boundary layer, whichever is closer along that line of sight. The lowest frequencies (dotted) sense the plasma sheet or lowest-density boundary layer, whichever is nearer.

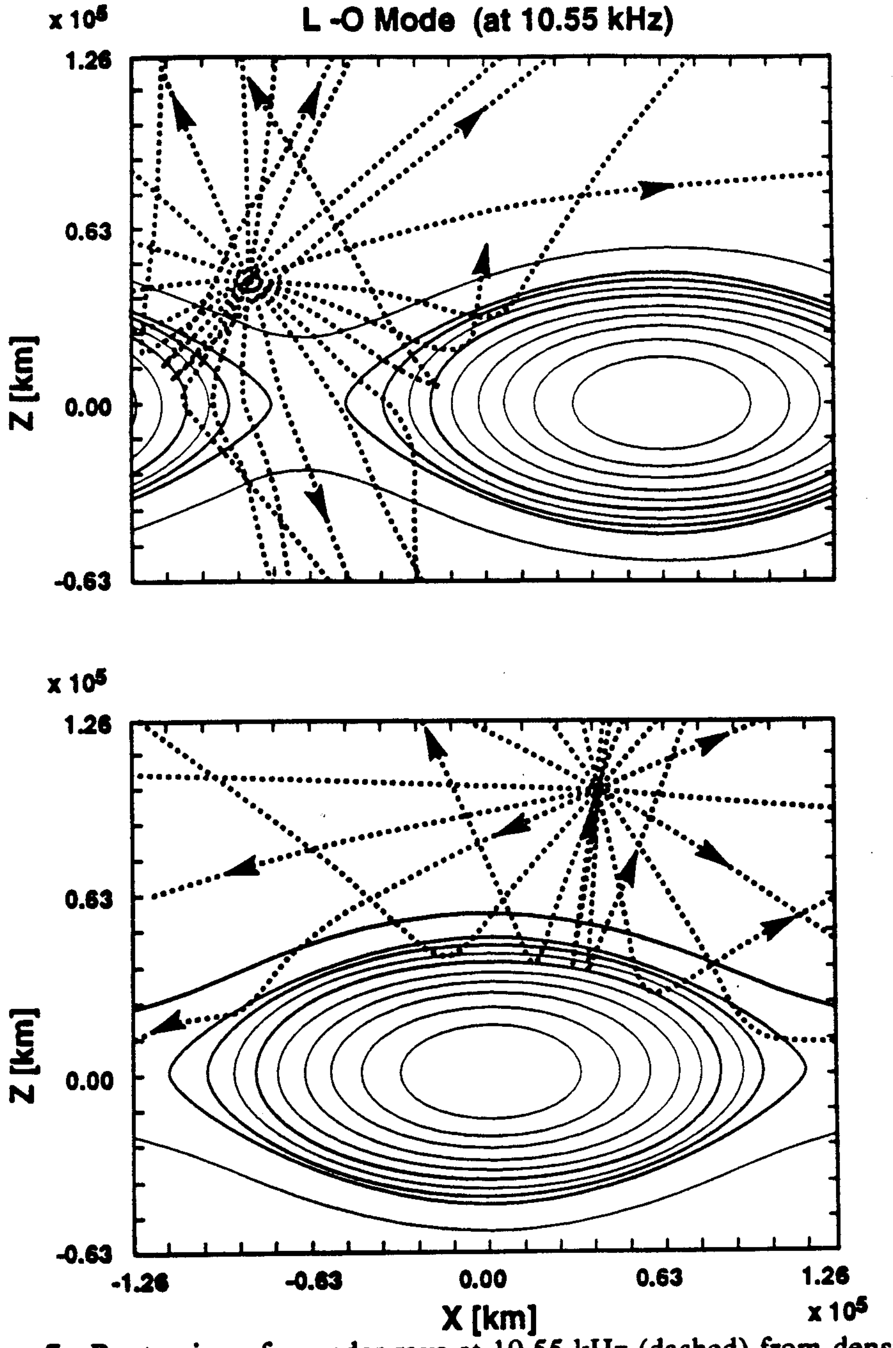

Figure 7. Raytracing of sounder rays at 10.55 kHz (dashed) from density gradients associated with a plasmoid. The plasmoid density contours and raytracing techniques are described in Omura and Green [1993]. The top panel indicates the reflections observed if the sounder is situated above an x-line; the bottom panel indicates the reflections observed if a plasmoid passes under the sounder.

Higher sounding frequencies can penetrate the plasmoid and may allow sounding of the far side magnetopause. Figure 8 shows a raytracing at 14 kHz (corresponding to 2.4 cm^{-3} density), the minimum frequency which will traverse the plasmoid. Higher frequency pulses will exhibit less refraction than shown here. The return signal from the far magnetopause will be weak, since the reflecting surface is far away; however, the signal should be focused from the concave nature of the magnetopause and may well be detectable.

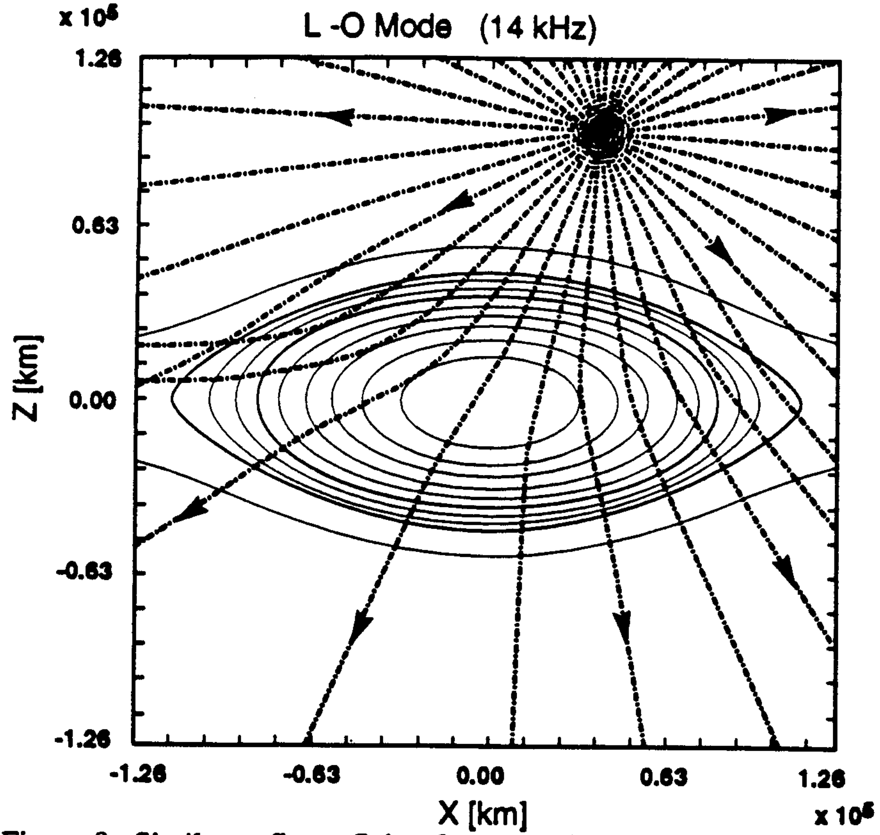

Figure 8. Similar to figure 7, but for a sounder frequency of 14 kHz (corresponding to 2.4 cm^{-3}), just above the plasma frequency in the center of the plasmoid. This frequency (and all higher frequencies) will penetrate the plasmoid and can be used to sense the distant magnetopause. Higher frequency rays will be refracted less than shown here.

CONCLUSIONS

A magnetospheric radio sounder can provide quantitative electron density profiles simultaneously in several different directions. From a sequence of these profiles, contour plots of the density structure in the orbital plane can be constructed, with some out-of-plane information as well. This capability will allow the remote sensing of magnetospheric topology and plasma domains on minute time scales. The application of the sounder technique to substorm studies is straightforward and powerful. If the density contrast between the plasmoid and the background lobe plasma is sufficient (and it should be in cislunar space), a sounder in an appropriate location should be able to monitor plasmoid formation, growth and motion and thus remotely sense major substorm reconfigurations in the magnetotail.

ACKNOWLEDGMENTS

We would like to acknowledge early discussions of this idea with Stan Shawhan, who gave us (PHR and JLG) strong encouragement. We acknowledge helpful discussions with David Winningham and Roger Anderson. The work at Rice University was supported by NASA under grant NAGW 1655, and at Nichols Research Corporation under contract 507854-f.

REFERENCES

Baker, D. N., R. C. Anderson, R. D. Zwickl, and J. A. Slavin, Average plasma and magnetic field variations in the distant magnetotail associated with near-Earth substorm effects, *J. Geophys. Res.*, *92,* 71-81, 1987.

Benson, R. F., Auroral kilometric radiation: Wave modes, harmonics, and source region electron densities, *J. Geophys. Res.*, *90,* 2753-2784, 1985.

Berkner, L. V., The international geophysical year, *Proc. IRE,* 47, 133-136, 1959.

Breit, G., and M. A. Tuve, A test for the existence of the conducting layer, *Phys. Rev.*, *28,* 554-575, 1926.

Buchau, J., B. W. Reinisch, D. N. Anderson, E. J. Weber, and C. Dozois, Polar cap plasma convection measurements and their relevance to the modeling of the high-latitude ionosphere, *Radio Sci.*, *23,* 521-536, 1988.

Calvert, W., R. F. Benson, D. L. Carpenter, S. F. Fung, D. Gallagher, J. L. Green, P. H. Reiff, B. W. Reinisch, M. F. Smith, and W. W. L. Taylor, The feasibility of radio sounding of the magnetosphere, to be submitted to *J. Geophys. Res.*, 1994.

Carpenter, D. L., B. L. Giles, C. R. Chappell, P. M. E. Decreau, R. R. Anderson, A. M. Persoon, A. J. Smith, Y. Corcuff, and P. Canu, Plasmasphere dynamics in the duskside bulge region: a new look at an old topic, *J. Geophys. Res.*, *98,* 19,243-19,271, 1993.

Carpenter, D. L., Whistler evidence of a "knee" in the magnetospheric ionization density profile, *J. Geophys. Res.*, *71,* 693, 1966.

Chen, F. F., *Introduction to Plasma Physics*, Plenus Press, N.Y., 1974.

Dyson, P. L. and J. D. Winningham, Top side ionospheric spread F and particle precipitation in the day side magnetospheric clefts, *J. Geophys. Res.*, *79,* 5219, 1974.

Fairfield, D. H., On the structure of the distant magnetotail: ISEE-3, *J. Geophys. Res.*, *97,* 1403-1410, 1992.

Franklin, C. A., and M. A. Maclean, The design of swept-frequency topside sounders, *Proc. IEEE, 57,* 897-929, 1969.

Fung, S. F., R. F. Benson, J. L. Green, M. F. Smith, D. L. Carpenter , W. Calvert, D. L. Gallagher, P. H. Reiff, B. W. Reinisch, and W. W. L. Taylor, Probing the Magnetopause and Boundary Layers by the Radio Sounding Technique, *J. Geophys. Res.*, submitted, 1994.

Green, J. L., and S. F. Fung, Radio sounding of the magnetosphere from a lunar-based VLF array, *Adv. Space Res.*, *14,* 217-221, 1994.

Green, J. L., R. F. Benson, W. Calvert, S. F. Fung, P. H. Reiff, B. W. Reinisch, and W. W. L. Taylor, A Study of Radio Plasma Imaging for the proposed IMI mission, NSSDC Technical Publication, Goddard Space Flight Center, February, 1993.

Green, J. L., R. F. Benson, D. L. Carpenter, W. Calvert, S. F. Fung, D. Gallagher, P. H. Reiff, B. W. Reinisch, M. Smith, and W. W. L.. Taylor, Radio sounding of the magnetosphere, to be submitted to *J. Geophys. Res.*, 1994.

Hoegy, W. R., and R. F. Benson, DE/ISIS conjunction comparisons of high-latitude electron density features, *J. Geophys. Res.*, *93,* 5947-5954, 1988.

Hones, E. W., Jr., Transient phenomena in the magnetotail and their relationship to substorms, *Space Sci. Rev.*, 23, 393, 1979.

Huang, X., and B. W. Reinisch, Automatic calculation of electron density profiles from digital ionograms. 2. True height inversion of topside ionograms with the profile-fitting method, *Radio Science, 17,* 837-844, 1982.

Hunsucker, R. D., *Radio Techniques for Probing the Terrestrial Ionosphere,* Vol. 22, Phys. Chem. Space, Springer Verlage, Berlin, 1991.

Jackson, J. E., E. R. Schmerling, and J. H. Whitteker, Mini-review on topside sounding, *IEEE Trans. Antennas Propagat., AP-28*, 284-288, 1980.

Lui, A. T. Y., and C. D. Anger, Uniform belt of diffuse auroral emissions seen by the ISIS 2 scanning photometer, *Planet. Space Sci., 21,* 799-809, 1973.

Nelms, G. L., and G. E. K. Lockwood, Early results from the topside sounder in the Alouette II satellite, in *Space Research VII,* edited by R. L. Smith-Rose, EB pp. 604-623, North-Holland Publishing Co., Amsterdam, 1966.

Omura, Y. and J. L. Green, Plasma wave signatures in the magnetotail reconnection region: MHD simulation and ray tracing, *J. Geophys. Res., 98,* 9189-9199, 1993.

Paschmann, G., N. Sckopke, G. Haerendel, I. Papamastorakis, S. J. Bame, J. R. Asbridge, J. T. Gosling, E. W. Hones Jr. and E. R. Tech, ISEE plasma observations near the subsolar magnetopause, *Space Sci. Rev., 22,* 717-737, 1978.

Paschmann, G., Plasma and particle observations at the magnetopause: implications for reconnection, in *Magnetic Reconnection in Space and Laboratory Plasmas,* Geophys. Monogr. Ser., *30,* edited by E. W. Hones Jr., pp. 114-123, AGU Press, Washington, D.C., 1984.

Petrinec, S. M., and C. T. Russell, External and internal influences on the size of the dayside terrestrial magnetosphere, *Geophys. Res. Lett., 20,* 339, 1993a.

Petrinec, S. M., and C. T. Russell, An empirical model of the size and shape of the near-earth magnetotail, *Geophys. Res. Lett., 20,* 2695, 1993b.

Ratcliffe, J. A., *The magneto-ionic theory and its application to the ionosphere,* 206 pp., Cambridge University Press, New York, 1959.

Reiff, P. H., Magnetopause Mapper (Ionosonde), Section 6.5, *Space Physics Missions Handbook,* ed. R. A. Cooper and D. H. Burks, NASA OSSA, 1991.

Reiff, P. H., J. L. Green, R. F. Benson, D. L. Carpenter, W. Calvert, S. F. Fung, D. L. Gallagher, B. W. Reinisch, M. F. Smith and W. W. L. Taylor, Radio imaging of the magnetosphere, *EOS, Trans. AGU, 75,* 129-134, 1994.

Reinisch, B. W., New techniques in ground-based ionospheric sounding and studies, *Radio Science, 21,* 3, pp. 331-341,1986.

Reinisch, B. W., D. M. Haines, and W. S. Kuklinski, The new portable Digisonde for vertical and oblique sounding, AGARD Proceedings Number 502, pp. 11-1 to 11-11, 1992.

Richardson, I. G. and S. W. H. Cowley, Plasmoid-associated energetic ion bursts in the distant geomagnetic tail, in *Magnetotail Physics,* edited by A. T. Y. Lui, pp. 251-256, The Johns Hopkins University Press, Baltimore, 1987.

Roelof, E. C. and D. G. Sibeck, The magnetopause shape as a bivariate function of IMF Bz and solar wind dynamic pressure, *J. Geophys. Res., 98,* 21,421-21,450, 1993.

Rosenbauer, H., H. Grunwaldt, M. D. Montgomery, G. Paschmann and N. Sckopke, Heos 2 plasma observations in the distant polar magnetosphere: The plasma mantle, *J. Geophys. Res., 80,* 2723-2737, 1975.

Russell, C. T. and R. L. McPherron, The magnetotail and substorms, *Space Sci. Rev., 15,* 205, 1973.

Sckopke, N., G. Paschmann, G. Haerendel, B. U. Ö. Sonnerup, S. J. Bame, T. G. Forbes, E. W. Hones, Jr., and C. T. Russell, Structure of the low-latitude boundary layer, *J. Geophys. Res., 86,* 2099-2110, 1981.

Shepherd, G. G., J. H. Whitteker, J. D. Winningham, J. H. Hoffman, E. J. Maier, L. H. Brace, J. R. Burrows, and L. L. Cogger, The topside magnetospheric cleft ionosphere observed from the ISIS 2 spacecraft, *J. Geophys. Res., 81,* 6092-6102, 1976.

Sibeck, D. G., R. A. Lopez, and E. C. Roelof, Solar wind control of the magnetopause shape, location, and motion, *J. Geophys. Res., 96,* 5489-5496, 1991.

Slavin, J. A., et al., CDAW 8 observations of plasmoid signatures in the geomagnetic tail: An assessment, *J. Geophys. Res., 94,* 15,153-15,175, 1989.

Slavin, J. A., M. F. Smith, E. L. Mazur, D. N. Baker, E. W. Hones, Jr., T. Iyemori, and E. W. Greenstadt, ISEE 3 observations of traveling compression regions in the Earth's magnetotail, *J. Geophys. Res., 98,* 15,425-15446, 1993.

Song, P., R. C. Elphic, C. T. Russell, J. T. Gosling, and C. A. Cattell, Structure and properties of the subsolar magnetopause for northward IMF: ISEE observations, *J. Geophys. Res., 95*, 6375-6387, 1990.

Spiro, R. W., M. Harel, R. A. Wolf, and P. H. Reiff, Quantitative simulation of a magnetospheric substorm, 3. Plasmaspheric electric fields and evolution of the plasmapause, *J. Geophys. Res.*, *86*, 2261-2272, 1981.

Whitteker, J. H., L. H. Brace, E. J. Maier, J. R. Burrows, W. H. Dodson, and J. D. Winningham, A snapshot of the polar ionosphere, *Planet. Space Sci., 24*, 25-32, 1976.

Williams, D., E. C. Roelof, and D. G. Mitchell, Global magnetospheric imaging, *Rev. Geophys.*, *30,* 183-208, 1992.

Wright, J. W., and R. D. Hunsucker, Estimation of turbulent energy dissipation, winds, and ionospheric structures from Dynasonde measurements, *Radio Sci.*, *18,* 988-994, 1983.

DRAFT MANUSCRIPT - Direct comments to W. Calvert, 319-337-6368 or 319-335-0564.

FEASIBILITY OF RADIO SOUNDING IN THE MAGNETOSPHERE

by

W. Calvert[1], R. F. Benson[2], D. L. Carpenter[3], S. F. Fung[2],
D. L. Gallagher[4], J. L. Green[2], D. M. Haines[6], P. H. Reiff[5],
B. W. Reinisch[6], M. F. Smith[2], and W. W. L. Taylor[7]

May 20, 1994

Abstract. A radio sounder for the magnetosphere would provide nearly-continuous observations of the plasmapause and magnetopause, as well as cross-sectional density images of the plasmasphere, cusp, and auroral plasma cavity. Operating at frequencies of a few kilohertz to a few megahertz with 500-meter tip-to-tip dipole antennas and ten watts transmitter power, such a sounder would be capable of about 10% density resolution and 500 km spatial resolution in a few minutes at distances of four earth radii. A sounder for the magnetosphere is therefore quite feasible and could revolutionize magnetospheric research by providing detailed observations of its principal density structures.

1. INTRODUCTION

Radio sounding involves detecting the echoes produced by wave reflections in a plasma at the plasma and extraordinary-mode cutoff frequencies. It thus measures density at a distance and is therefore ideal for measuring the density structure of the magnetosphere.

A radio sounder uses a pulsed radio transmitter and radio receiver to measure the echo delay versus frequency, since this determines the density as a function of distance from the sounder. Operating over a suitable range of frequencies, a magnetospheric sounder could thus

---

[1] University of Iowa, Iowa City, IA 52242

[2] Goddard Space Flight Center, Greenbelt, MD 20771

[3] Stanford University, Stanford, CA 94305

[4] Marshall Space Flight Center, Huntsville, AL 35812

[5] Rice University, Houston, TX 77251

[6] University of Massachusetts at Lowell, Lowell, MA 01854

[7] Nichols Research Corp., Arlington, VA 22209

produce continuous density measurements as a function of orbital position, yielding complete, two-dimensional, cross-sectional density images of the magnetopause, plasmapause, plasmasphere, polar cusp, and auroral cavity, as shown in Figure 1.

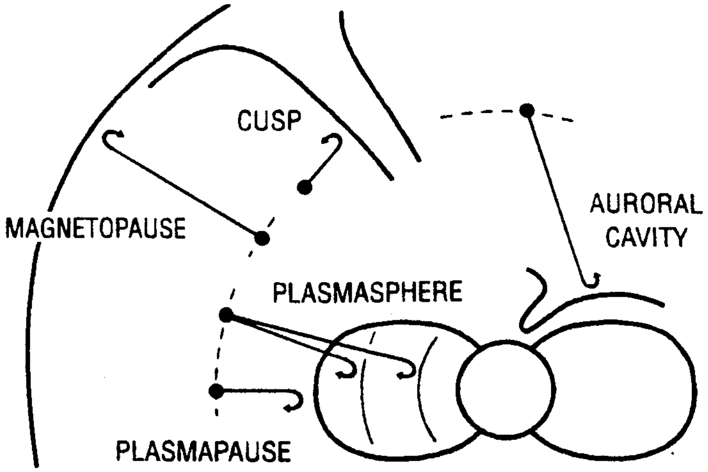

Fig. 1. Principal targets for magnetospheric sounding

Pioneered for the ionosphere during the 1920's and 30's by Breit and Tuve [1926], Appleton [1932], Ratcliffe [1933], and others, radio sounding using a world-wide network of modern digital ionosondes has since become one of the main tools of ionospheric research [Davies, 1990; Reinisch, 1986; Reinisch, et al., 1992]. Satellite radio sounding also became one of the first major techniques used in space research during the highly-successful Alouette and ISIS topside-sounder programs of 1960's and 70's [Schmerling and Langille, 1969; Franklin and Maclean, 1969].. Radio sounding has thus had a long and successful history, and it promises equal success for the magnetosphere [Calvert, et al., 1972; Calvert, 1981b; Reiff, et al., 1994; Green and Fung, 1993; Green, et al., 1993].

A magnetospheric sounder would presumably appear as shown in Figure 2, using three orthogonal dipole antennas to launch radio pulses, receive their echoes, and to measure echo delay and direction. Antenna length is critical for radio sounding, and tip-to-tip antenna lengths of 500 meters for two antennas in the satellite spin plane, and 10 meters for a third antenna along the spin axis, have been assumed for this study.

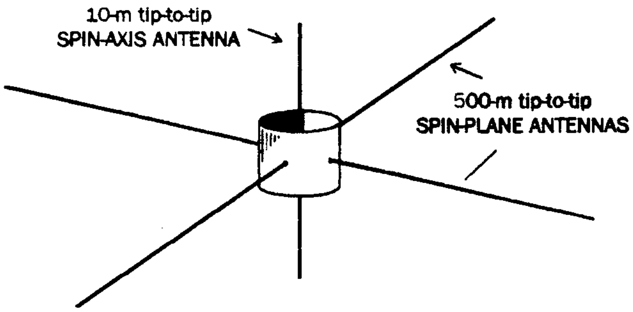

Fig. 2. Magnetospheric sounder, using two long transmit/receive dipoles in the spin plane and a short spin-axis dipole for reception only.

In order to determine the feasibility of radio sounding it is necessary to estimate the echo strengths which can be produced by a sounder and determine the resulting density precision and spatial and temporal resolution. The characteristics of radio echoes will thus be discussed in the following section, followed by discussions of pulse transmission and echo reception in Sections 3 and 4, and an analysis precision and resolution in Section 5. The conclusions will then be presented in Section 6.

2. ECHO CHARACTERISTICS

The radio echoes used in sounding are produced at wave cutoffs where the refractive index goes to zero and total internal reflection occurs [see Ratcliffe, 1959; Budden, 1985; Stix, 1962; Allis, et al., 1963]. As a result, reflection is lossless and coherent, and the echoes are produced perpendicular to the refractive index contours at the point of reflection. Echo directions are thus determined by the density distribution of the target plasma, and are often perpendicular to the magnetic field at interfaces like the plasmapause and magnetopause where magnetic forces control the density.

2.1. Frequency

A sounder launches two waves of opposite elliptical polarization known as the ordinary and extraordinary waves. These two waves propagate independently and produce separate echoes which can be distinguished by their different delay, doppler shift, and polarization. The plasma density can be determined from either echo, and if both are observed with sufficient precision, they can be used to measure the magnetic field strength at the point of reflection.

The cutoff frequency of the ordinary mode is the plasma frequency

$$f_p = \frac{1}{2\pi}\sqrt{\frac{N_e e^2}{\epsilon_0 m}} = 8.98\sqrt{N_e}\ kHz \tag{1}$$

where N_e is the electron density per cubic centimeter, e and m are the electronic charge and mass, and ε_0 is the permittivity of free space. The cutoff of the extraordinary mode occurs at a frequency only somewhat higher throughout most of the magnetosphere, given by

$$f_x = \sqrt{f_p^2 + f_g^2/4} + f_g/2 \tag{2}$$

where

$$f_g = \frac{eB}{2\pi m} = 28\,B\ kHz \tag{3}$$

is the electron cyclotron frequency and B is the magnetic field strength in microtesla.

Since plasma densities in the magnetosphere range from less than 0.1 cm^{-3} in the auroral cavity and tail lobes to 10^4 cm^{-3} or more in the topside ionosphere, the plasma frequency in the magnetosphere ranges from about 3 kHz to over 1 MHz. Magnetic field strengths, on the other hand, range from about 30-50 microtesla in the ionosphere to about 30 nanotesla at the magnetopause, and even less in the geomagnetic tail. The cyclotron frequency thus ranges from about 1.5 MHz in the ionosphere to less than one kilohertz at the magnetopause, and except in the auroral plasma cavity [see Calvert, 1981a], it is generally less than the plasma frequency. The pertinent frequencies for radio sounding in the magnetosphere therefore range from a few kHz to a few MHz.

2.2 Echo Delay

Although the phase velocities of the pertinent ordinary and extraordinary waves are greater than the speed of light, the group velocity v_g which determines the speed of pulse propagation (neglecting magnetic effects) is approximately

$$v_g = c\sqrt{1 - f_p^2/f^2} \tag{4}$$

where f is the frequency, c is the speed of light, and f_p is the local plasma frequency. Since the plasma frequency along most of the echo path is usually much less than the sounding frequency, the group speed is nearly the speed of light, and the round-trip echo delay is approximately 2/c times the distance, or about 43 milliseconds per earth radii (R_E). Echo delays in the magnetosphere, at distances of up to a few earth radii, thus range from a few tenths of a second to a half second or more.

2.3. Echo Power Flux

In order to estimate echo signal strengths for a sounder, it is necessary to calculate the echo power flux Φ_e (in watts per square meter) which results from a given effective radiated sounder power P, in the direction of the target, as follows.

2.3.1. Planar Target. For a planar target, as shown in Figure 3, the power flux Φ_x at the point of reflection is

$$\Phi_x = \frac{P}{4\pi s^2} \tag{5}$$

where P is the effective radiated power and s is the target distance. Since reflection is coherent, this flux spreads out over a larger arc y = 2x when it returns to the sounder. Considering both dimensions of the echo wave front, the echo power flux Φ_{eo} at the sounder is therefore

$$\Phi_{eo} = \left(\frac{x}{y}\right)^2 \Phi_x = \frac{P}{16\pi s^2} \tag{6}$$

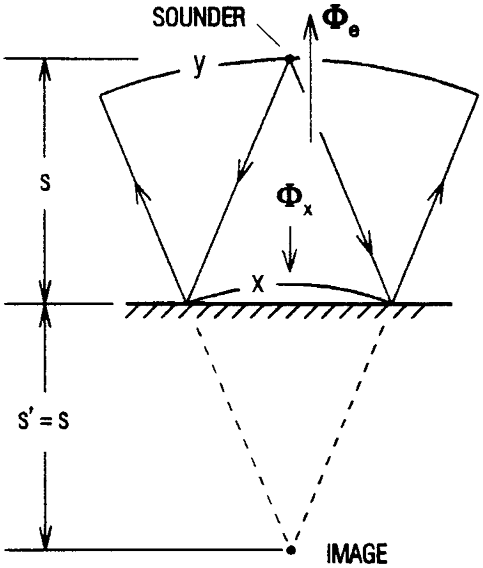

Fig. 3. Echo produced by a planar target where s is the target distance, Φ_x is the power flux at reflection, and Φ_e is the returning echo flux.

2.3.2. Curved Targets. In the magnetosphere, however, the target radii of curvature are frequently comparable to the echo distance, and it is therefore necessary to determine the echo power flux for curved targets, as follows.

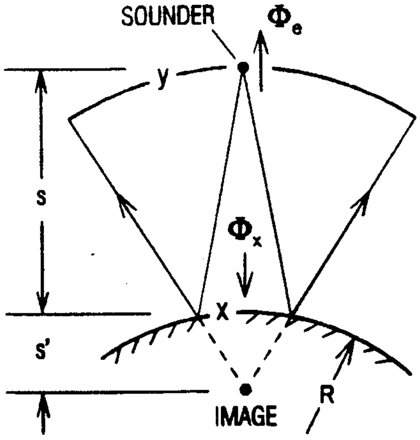

Fig. 4. Echo for a curved target, where R is the surface radius of curvature and s' is the image distance.

For a curved surface, the echo geometry becomes that in Figure 4, where s and s' are the object and image distances determined by the spherical mirror equation of geometric optics:

$$\frac{1}{s'} - \frac{1}{s} = \frac{2}{R} \tag{7}$$

where R is the surface radius of curvature, positive for a convex surface like the equatorial plasmapause and negative for concave surfaces like the magnetopause (for a sounder in between these two regions). Since the arcs x and y in Figure 4 subtend the same angle at the image of the source:

$$\frac{y}{x} = \frac{s + s'}{s'} = 2\,(1 + s/R) \tag{8}$$

Again considering both echo dimensions, the echo power flux thus becomes

$$\Phi_e = \frac{P}{16\,\pi\,s^2\,|1 + s/R_1|\,|1 + s/R_2|} \tag{9}$$

where R_1 and R_2 are the principal radii of curvature of the surface. The absolute-value bars in this equation are needed to keep the power flux positive for the case of a sounder outside the center of curvature of concave surface, since R is then negative with s greater than -R.

Equation 9 is the equivalent of the radar equation for targets of arbitrary size. For a large target where R >> s, it becomes Equation 6 for a planar target, whereas for a small target (R << s), it becomes $\Phi_e = P(\pi R_1 R_2)/(4\pi s^2)^2$, which is the classical radar equation for a target cross-section of $\pi R_1 R_2$, which is the area of an ellipse with R_1 and R_2 as its semi-major and semi-minor axes. This formula applies to both regimes in the geometric approximation where the reflecting surfaces are smooth on the scale of a wavelength. In the large-target or "planar" approximation it applies to targets larger across than a Fresnel zone, given by $(2\lambda s)^{1/2}$, where s is the target distance and λ is the wavelength. See Davies [1990] for a one-dimensional version of this formula which is applicable to ionospheric focusing.

Except for small-scale irregularities like those which occur in the auroral zone and at the plasmapause under certain conditions, Equation 9 should be a good approximation for the echo strengths produced by a sounder. Moreover, since such irregularities tend to produce stronger echoes which can also be analyzed for density [see Calvert and Schmidt, 1964], it is also a worst-case approximation for the minimum usable echoes produced by a sounder.

2.4. *Relative Flux*

Echo strengths for the magnetopause, plasmapause, and plasmasphere will be calculated by first determining Φ_e/P, then multiplying by the sounder power P in the direction of the target. Φ_e/P will be called the *relative echo flux*, and it represents the effect of echo geometry, in units of inverse meters squared, independently of sounder power. The relative flux, which depends only upon s, R_1, and R_2, will be calculated in this section, and P will be calculated in Section 3.

2.4.1. *Magnetopause*. As shown in Figure 1, the magnetopause will be approximated by a 10-R_E earth-centered sphere, and the sounder radial distance will be assumed to be 6 R_E. The echo distance and surface radii curvature are therefore s = 4 R_E and $R_1 = R_2 = -10\ R_E$. The relative echo flux, according to Equation 9, is thus about $8.5 \times 10^{-17}\ m^{-2}$, independent of frequency, since the magnetopause is abrupt, and also independent of echo position, since in this approximation the sounding distance and radii of curvature are constant.

For magnetopause distances of 8 and 12 R_E, the relative fluxes become 2.1×10^{-16} and $5.4 \times 10^{-17}\ m^{-2}$; which vary by less than $1/s^2$ because of increased focusing at greater distances. Such focusing, which results from the s/R terms in Equation 9 for R negative and greater than s, yields echo fluxes about two to four times stronger than for a planar target at the same distance. As a result, these echoes are significantly stronger than plasmapause echoes at the same distance, which tend to be defocused by comparable factors.

The actual curvature of the magnetopause will also vary with echo position, gradually decreasing along the flanks of the magnetosphere. This will cause multiple echoes, and frequently up to five such echoes should occur, coming from front, left, right, up, and down with respect to the solar wind and the magnetic axis of the Earth. Multiple echoes are also expected from ripples on the magnetopause, sometimes producing intense focusing as the sounder passes near a ripple center of curvature. Such multiple echoes, which would be of great benefit in determining the shape and behavior of the magnetopause, should be easily distinguishable from one another by their different delays and doppler shifts, and their directions and distances can be measured independently, as discussed below.

In addition, when the echo path misses the earth and plasmasphere, echoes should also sometimes be detectable from the night hemisphere, at distances of roughly 16 R_E, with focusing gains of about 3 and relative echo fluxes of about $5 \times 10^{-18}\ m^{-2}$. From a satellite at 6 R_E, the magnetopause thus should be detectable more-or-less continuously for hours a time, and sometimes for nearly whole orbits outside the plasmasphere.

2.4.2. Plasmapause. Although the actual plasmapause may be quite different, it will be modeled as an L = 4 L-shell, as shown in Figure 5. The shape of the plasmapause thus becomes

$$r = L \cos^2 \lambda \tag{10}$$

where r is the radius and λ is the magnetic latitude, and the magnetic dip angle I is given by

$$\tan I = 2 \tan \lambda \tag{11}$$

In terms of this dip angle and the radial distance, it can be shown that the radius of curvature in the magnetic meridian becomes

$$R_1 = \frac{2\,r}{(3\cos^2 I + 1)\cos I} \tag{12}$$

whereas that in the echo plane mutually perpendicular to the plasmapause and magnetic meridian at the point of reflection is

$$R_2 = \frac{2\,r \cos I}{3\cos^2 I - 1} \tag{13}$$

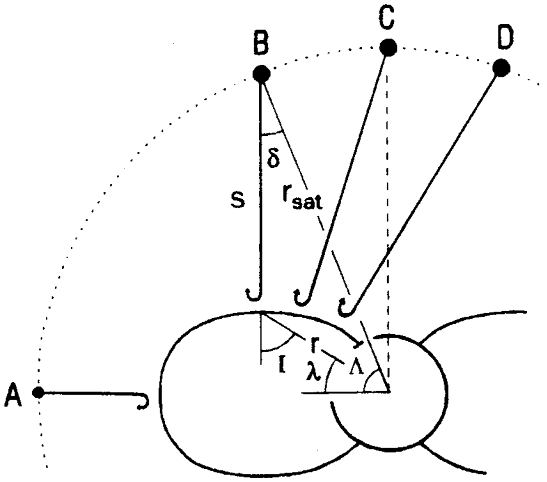

Fig. 5. Plasmapause echo geometry, where r, λ, and I are the radius, latitude, and dip angle; Λ and r_{sat} are the satellite latitude and radius; and s and δ are the echo distance and angle.

These two radii of curvature are shown in Figure 6 versus magnetic latitude. Notice in this figure that R_2 becomes infinite for a magnetic latitude of 35.3°. This occurs where the dip angle equals the magnetic colatitude (position B in Figure 5), at the "top" of the plasmasphere, furthest from the magnetic equatorial plane. At this point, the azimuthal radius of curvature increases through infinity to become negative, and the plasmapause thus becomes concave in the azimuthal direction, like the inside of a donut hole. This causes focusing along the polar axis, as discussed below. The plasmapause thus changes from doubly-convex at the equator to a saddle-shaped surface at high latitudes, which is convex in one direction and concave in the other. Its radii of curvature, according to Equations 12 and 13, increase from $R_1 = 2\ R_E$ and $R_2 = 4\ R_E$ at the equator to $R_1 = 4.62\ R_E$ and $R_2 = \pm\infty$ at 35.3° magnetic latitude. Both then continue to increase (R_2 increasing from minus infinity) to become $R_1 = 5.86\ R_E$ and $R_2 = -0.72\ R_E$ at 60° latitude where $r = R_E$ and the plasmapause blends into the ionosphere.

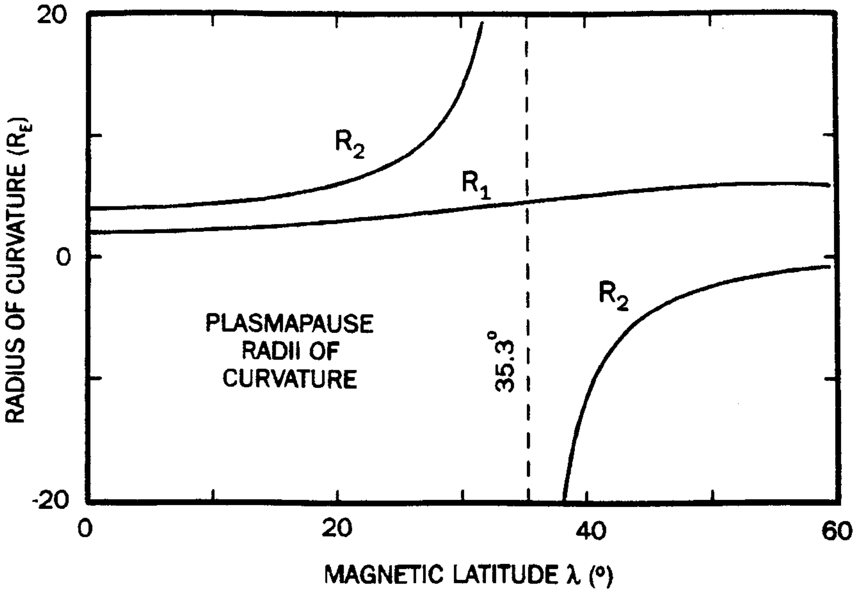

Fig. 6. Plasmapause radii of curvature: R_1 in the magnetic meridian and R_2 in the perpendicular to the magnetic meridian.

From the law of sines for the triangle at position B in Figure 5, the echo distance s, perpendicular to the plasmapause for a sounder at a constant geocentric altitude r_{sat}, varies with the satellite magnetic latitude Λ, as follows:

$$s = \frac{\sin(I - \delta)}{\sin I}\, r_{sat} \tag{14}$$

where $\delta = I + \lambda - \Lambda$ is the echo deviation angle shown in Figure 5, given by

$$\delta = \sin^{-1}\left(\frac{r}{r_{sat}} \sin I\right) \tag{15}$$

The quantities r, I, R_1, and R_2 can thus be computed for a given magnetic latitude from Equations 10-13, δ then can be computed from Equation 15, and finally, s can be computed from Equation 14. The relative echo flux can then be determined from Equation 9 and plotted against $\Lambda = I + \lambda - \delta$, as shown in Figure 7. The positions labeled A through D in Figure 5 correspond to A through D in this figure.

The relative echo flux from the plasmapause for a sounder at 6 R_E thus decreases from about 4.1×10^{-17} m^{-2} at the equator to a minimum of 1.6×10^{-17} m^{-2}, slightly poleward of position B. It then increases to infinity along the axis of the plasmasphere (position C), since for a figure of revolution, this is automatically where the azimuthal center of curvature always occurs. Although for a symmetrical plasmasphere this corresponds to echoes coming from a continuous ring around the pole, the predicted focusing should still occur even if the plasmasphere is not exactly symmetrical, at those spots near the pole where the satellite is at the local center of curvature. The echoes from C to D then correspond to sounding the plasmapause from the other side of the polar axis, at progressively lower altitudes until it merges with the ionosphere and the echoes disappear. The dashed curve in Figure 7 represents the same variation measured from the equator on the opposite hemisphere. Multiple echoes should therefore occur within about 10-20° of the polar axis, from high and low altitudes on opposite sides of the plasmasphere. Such echoes, which come from the plasmasphere at magnetic latitudes above about 35°, should be quite useful in determining the relationship between the auroral plasma cavity and the plasmapause.

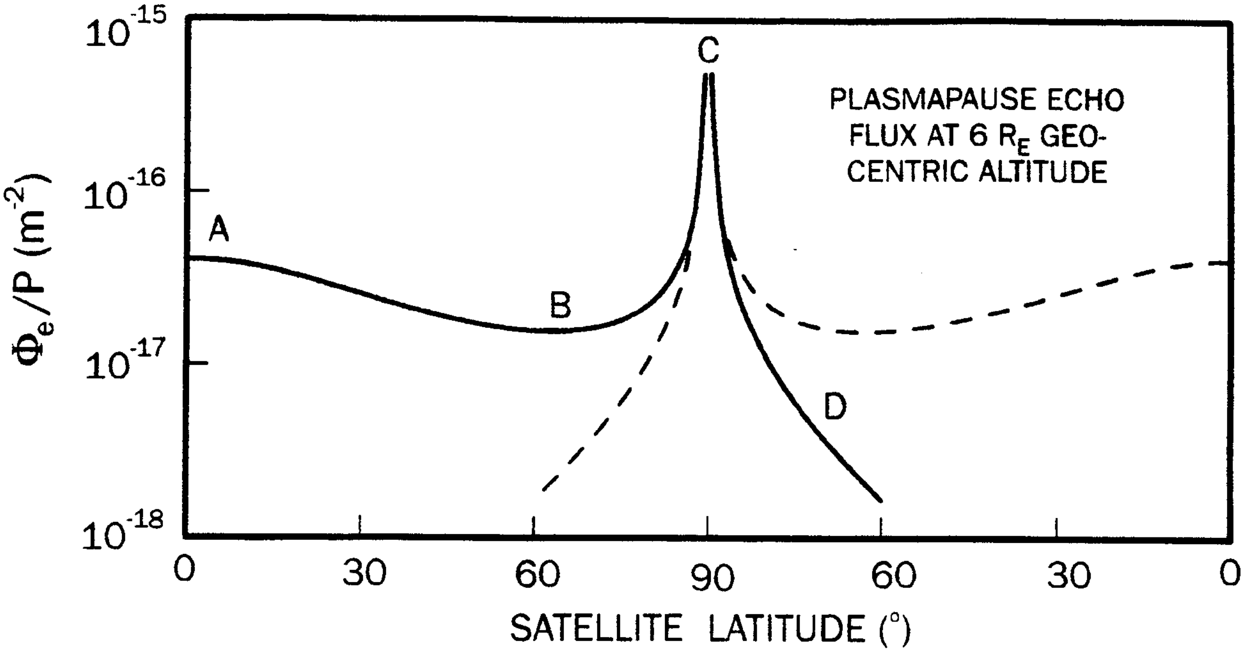

Fig. 7. Relative echo flux from the plasmapause, where A, B, C, and D pertain to Figure 5 and the dashed curve corresponds to a sounder in the opposite hemisphere.

*2.4.3. **Plasmasphere**.* The density contours within the plasmasphere should be different in shape than the plasmapause because of diffusive equilibrium. Instead of following the magnetic field, according to the density model of Carpenter and Anderson [1992; see also Carpenter, et al., 1993], they are approximately earth-centered, with the density typically varying from about 400 cm^{-3} at the equatorial plasmapause to about 2000 cm^{-3} at 2 R_E geocentric altitude. The echo direction should thus change abruptly as the echo point moves into the plasmasphere, as shown in Figure 1, and echoes from the plasmasphere should be detectable only within about ±60° from

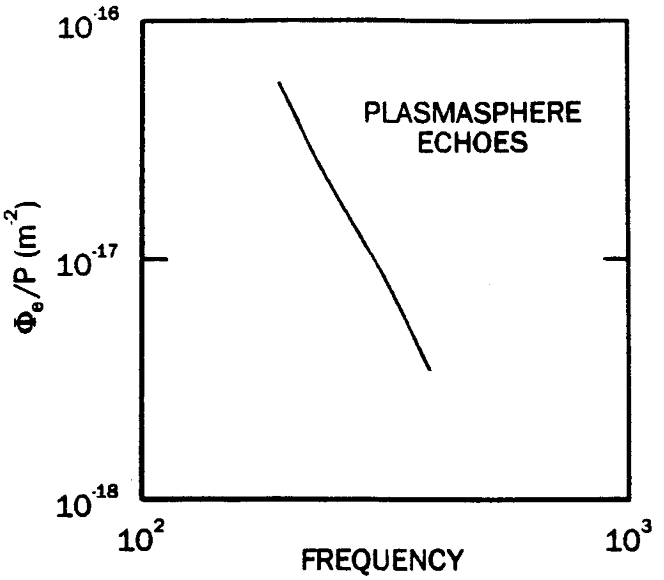

Fig. 8. Relative flux for the plasmasphere, for the density model of Carpenter and Anderson.

the equator. For a satellite at 6 R_E, the echo distance for echoes from the plasmasphere increases from 2 R_E to 4 R_E as the radius of curvature decreases from 4 R_E to 2 R_E. As a consequence, for the Carpenter-Anderson model, the relative echo flux varies from about 5.4 x 10^{-17} m^{-2} at 180 kHz to 3.4 x 10^{-18} at 400 kHz, as shown in Figure 8.

*2.4.4. **Summary**.* For the three principal sounding targets in the magnetosphere, the estimated relative echo fluxes Φ_e/P, for a satellite at 6 R_E, are as follows: For a nominal magnetopause at 10 R_E and the sounder in front of the Earth, the relative flux should be about 8.5 x 10^{-17} m^{-2}, and should vary by about a factor of 2 with magnetopause position. For a plasmapause extending to 4 R_E at the equator, the worst-case echo fluxes should be about 1.6 x 10^{-17} m^{-2}, and they should increase by about a factor of 2.5 from above the plasmasphere to the equator. Finally, for echoes from inside the plasmasphere, the relative fluxes should vary as shown in Figure 8. These will be used below to determine the nominal performance of a sounder in the magnetosphere.

3. *PULSE TRANSMISSION*

In order to determine absolute echo power fluxes, it is necessary to multiply the relative fluxes deduced above by the effective radiated power of the sounder transmitter. This calculation will be carried out in this section by analyzing the power which can be radiated by the two spin-plane antennas at the pertinent frequencies.

3.1. Equivalent Circuit

An equivalent circuit for pulse transmission is shown in Figure 9, where R_a is radiation resistance, X_a is the antenna reactance, and V_a is the root-mean-squared (rms) voltage at the root of the antenna. For this circuit the antenna current is

$$I_a = \frac{V_a}{\sqrt{R_a^2 + X_a^2}} \qquad (16)$$

and the power delivered to the radiation resistance and hence radiated by the antenna is therefore

$$P_t = I_a^2 R_a = \frac{R_a V_a^2}{R_a^2 + X_a^2} \qquad (17)$$

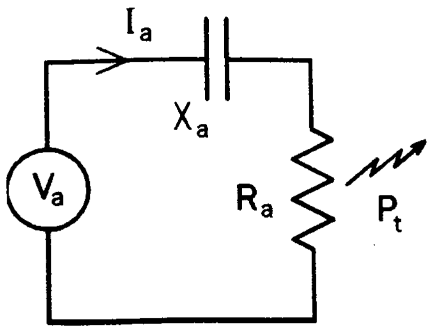

Fig. 9. Equivalent circuit for transmission, where R_a is the radiation resistance, X_a and is the antenna reactance.

According to Jordan [1950, Ch. 14], the reactance and radiation resistance of a short dipole antenna, in ohms, are given by

$$X_a = \frac{120}{\pi}\,[1 - \ln(L/2a)]\left(\frac{\lambda}{L}\right) \qquad (18)$$

and

$$R_a = 20\,\pi^2\left(\frac{L}{\lambda}\right)^2 \qquad (19)$$

where $\lambda = c/f$ is the wavelength, L is the tip-to-tip antenna length, and a is its radius. These are shown in Figure 10, along with their schematic behavior at higher frequencies, for a 500-meter wire antenna, 1 mm in diameter. Plasma effects on the antenna impedance and radiation for long-range echoes can usually be neglected, since the sounder operates at frequencies well above the local plasma and cyclotron frequencies.

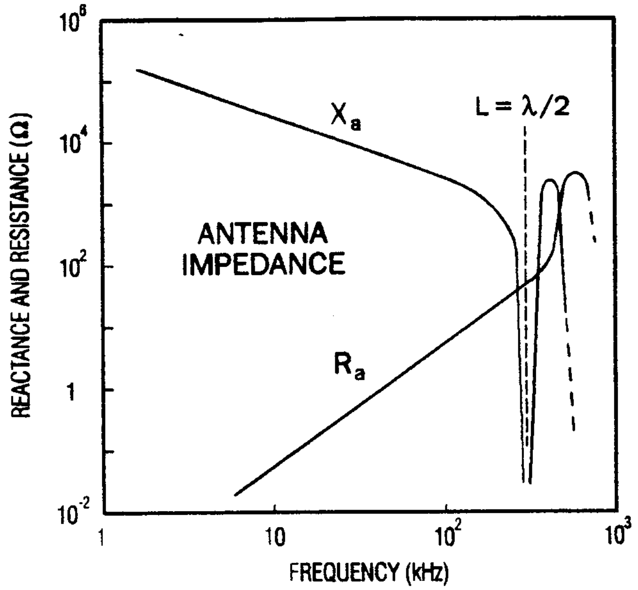

Fig. 10. Reactance and radiation resistance of a 500-meter wire dipole (schematic).

3.2. Radiated Power

As shown in Figure 10, below about 100 kHz the antenna reactance is quite large and increases toward lower frequencies as 1/f, whereas the radiation resistance is small and decreases as f^2. This severely limits the power that can be radiated at low frequencies. At 30 kHz, for example, the radiation resistance and reactance are approximately 0.5 Ω and 9000 Ω, respectively. The antenna current for V_a = 3000 volts is then only about 330 mA, and the radiated power is therefore only about 50 milliwatts. Although requiring careful engineering for space, high voltages are essential to radiate sufficient power at low frequencies, and for such a source, according to Equations 17-19, the radiated power for $X_a >> R_a$ becomes

$$P_t \approx \frac{R_a V_a^2}{X_a^2} = \frac{0.135\,(L_t/\lambda)^4\, V_{\max}^2}{[1 - \ln(L_t/2a)]^2} \qquad (20)$$

where L_t is the transmitting antenna length and $V_{\max}$ is the maximum allowed rms transmitter voltage at the root of the antenna.

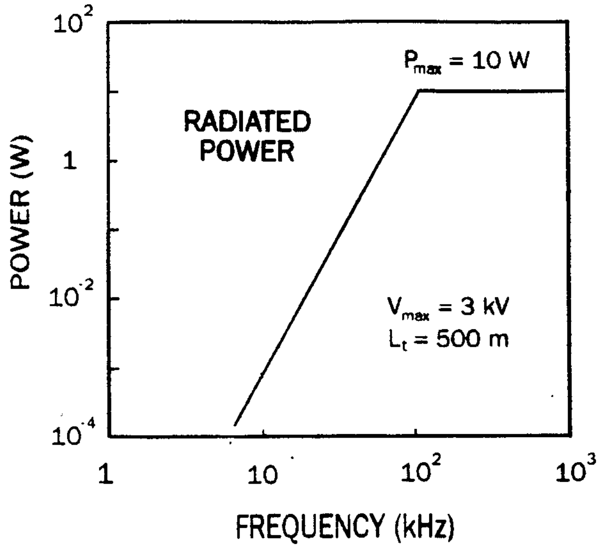

Fig. 11. Power radiated by a 10-watt, 3 kV transmitter using a 500-meter dipole antenna.

The power radiated as a function of frequency, for L_t = 500 m, a = 0.5 mm, and $V_{\max}$ = 3 kV, is shown in Figure 11, for an assumed maximum transmitter power of $P_{\max}$ = 10 watts. According to Equation 20, the crossover point between voltage and power limiting occurs at the frequency

$$f_x = \frac{1.65\,c}{L_t}\sqrt{\frac{\ln(L/2a) - 1}{V_{\max}}}\;\sqrt[4]{P_{\max}} \qquad (21)$$

which becomes about 112 kHz for the parameters given. This crossover frequency should be as low as possible for a high-performance sounder, and the 500-m antenna length was chosen to put this frequency down near the sounding frequencies necessary for a magnetospheric sounder. It varies inversely with the antenna length and the square-root of the antenna voltage, and the radiated power at lower frequencies varies as the fourth power of the frequency, according to Equation 20.

Since pulse transmission is assumed to be limited by the maximum feasible root antenna voltage, there is no need to tune the transmitting antenna, unless this is part of the technique used to produce the needed high voltages. It is therefore expected that a sounder transmitter for the magnetosphere will consist of a high-voltage source with active circuits to reduce the voltage when the power limit is reached. This design also makes it simpler to cope with the impedance variations at the higher frequencies in Figure 11.

The effective radiated power also depends on the antenna radiation pattern and on the polarization mismatch between the transmitted wave and the characteristic polarization of the wave mode producing an echo. The antenna pattern, according to Jordan [1950], yields between 50% power gain and 25% loss within about 45° of the antenna axis normal, and the pattern null along the antenna axis can be eliminated by switching between the two long spin-axis antennas at appropriate times for the echoes being received. For the low plasma densities at the sounder, the pertinent wave modes are approximately circular [see Allis, et al., 1963, Ch. 4]. Then, since the transmitted polarization of a dipole antenna is linear, polarization mismatch will reduce the transmitted wave signal by a factor of two. This, however, can also be compensated for by using both antennas at the same time. These two factors are therefore rather minor and can be neglected.

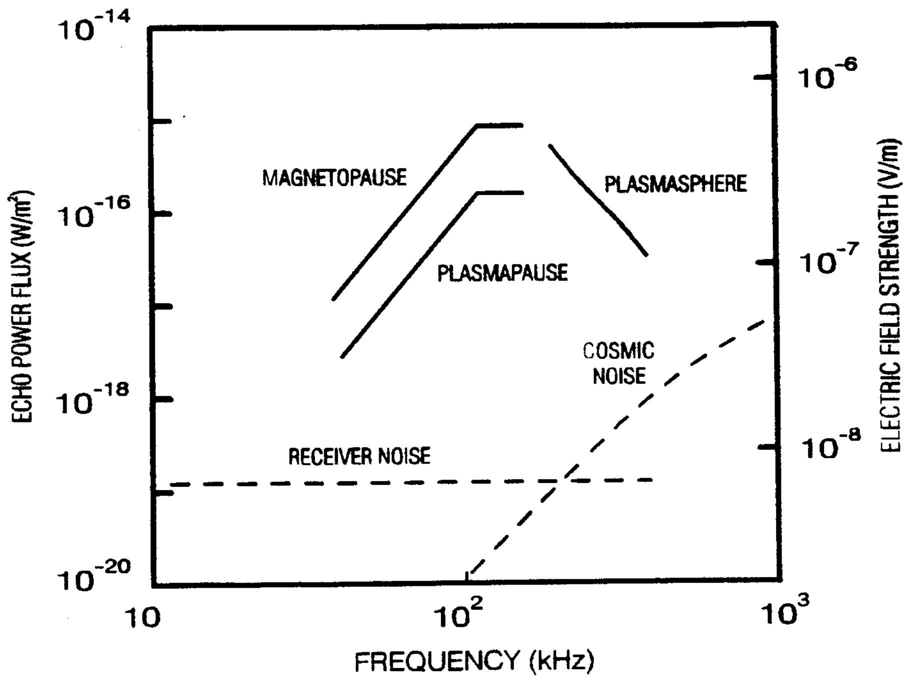

Fig. 12. Echo flux and reception thresholds for a 10-watt, 3-kV radio sounder at 6 R_E, using 500-meter transmitting and a 10-meter receiving antennas, and a 300 Hz bandwidth.

The expected power fluxes for the main sounding targets in the magnetosphere can then be calculated by multiplying the transmitted power in Figure 11 by the relative fluxes deduced above. These are shown in Figure 12, along with the reception thresholds determined in the next section. The scale on the right in this figure also indicates the corresponding wave field strength E, in volts/meter, given by $E^2 = 377\Phi_e$, where Φ_e is in W/m^2.

4. RECEPTION

Echo reception involves receiving the pertinent echoes in the presence of external and internal noise, and the threshold for reception is determined by this noise. It is therefore necessary to identify the relevant noise sources as a function of frequency, as follows.

4.1. Receiver Noise Threshold

4.1.1. Equivalent Circuit. The equivalent circuit for reception is shown in Figure 13, where R_a is the radiation resistance, X_a is the antenna reactance, R_i is the receiver input impedance, and L_x is a series inductance which has been included for tuning the antenna. For this circuit, the received echo signal appears as a power P_e in the radiation resistance, given by

$$P_e = \frac{V_e^2}{R_a} = \Phi_e \frac{\lambda^2}{4\pi} \qquad (22)$$

where λ is the wavelength, V_e is the echo voltage across the radiation resistance, and $\lambda^2/4\pi$ is the antenna intercept area [see Jordan, 1950, Ch. 12]. Without tuning ($L_x = 0$), the echo power P_r that reaches the receiver input terminals is then

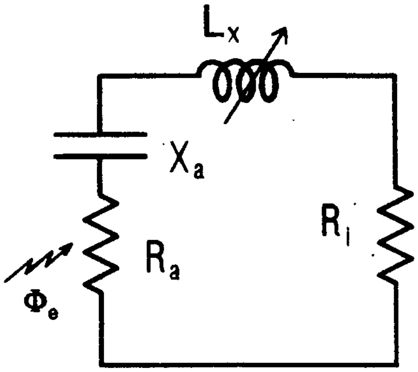

Fig. 13. Equivalent circuit for reception, where R_i is the receiver input impedance and L_x is an inductor for antenna tuning.

$$P_r = I_a^2 R_i = \frac{V_e^2 R_i}{X_a^2 + R_i^2} = \frac{\Phi_e \lambda^2}{4\pi}\left(\frac{R_i R_a}{X_a^2 + R_i^2}\right) \qquad (23)$$

Because of the small values of R_a and large values of X_a in Figure 10, tuning is essential for reception at low frequencies, as follows.

4.1.2. Antenna Tuning. With antenna tuning, in which L_x is adjusted to cancel X_a, the received power, according to Equations 18 and 23, becomes

$$P_r = \frac{\Phi_e \lambda^2 R_a}{4 \pi R_i} = \frac{5 \pi L_r^2 \Phi_e}{R_i} \tag{24}$$

where L_r is the receiving antenna length. Antenna tuning thus yields an echo signal power which is independent of frequency and increased by the large factor $(X_a/R_i)^2$. Such tuning, however, requires a tunable inductance of typically 50 mH for a 500-meter antenna at 30 kHz, and one of almost 3 henrys for a 10-meter antenna at the same frequency. Although the former should be relatively easy to implement with a bank of inductors and electronic switches, the latter poses an engineering challenge. This, however, is necessary so all three antennas can be used for reception to measure the echo directions.

4.1.3. Equivalent Noise Flux. The power P_n of receiver thermal noise is given by

$$P_n = q\, k\, T_i\, \Delta f \tag{25}$$

where q is the noise figure of the receiver (typically 3 or less for a good design), T is the Kelvin temperature of the receiver, $k = 1.38 \times 10^{-23}$ J/°K is Boltzmann's constant, and Δf is the receiver bandwidth (see Bennett [1960], or equivalent texts on electrical noise).

It is convenient to convert this into an equivalent noise flux as if the receiver noise were being received by the antenna. This is accomplished by equating P_n to P_r in Equation 25 and solving for $\Phi_e = \Phi_n$:

$$\Phi_n = \frac{q\, k\, T_i R_i \Delta f}{5 \pi L_r^2} \tag{26}$$

The thermal-noise threshold for $q = 3$, $T_i = 300°$ K, $\Delta f = 300$ Hz, $R_i = 50\ \Omega$, and $L_r = 10$ m thus becomes 1.2×10^{-19} W/m^2, independent of frequency, as shown in Figure 12. Since reception using the short spin-axis antenna will limit measuring echo directions out of the satellite spin plane, this worst-case threshold will be used to determine the signal-to-noise ratio in the following section. It should be noted, however, that the reception thresholds will be substantially lower for the two longer spin-plane antennas, and hence that the spin direction should be chosen to favor echoes arriving approximately in the spin plane.

4.1.4. External Noise. The principal external noise sources are cosmic radio noise, solar noise bursts, terrestrial continuum, and auroral kilometric radiation (AKR). Of these, the cosmic radio noise is weakest and represents the minimum unavoidable noise floor for radio sounding, since it is steady, uniform in frequency and space, and always present. This noise, from the measurements of Bougeret, et al. [1984], is shown in Figure 12 for a bandwidth of 300 Hz.

Solar noise bursts are generated intermittently as a result of solar flares, and are often strong enough to preclude radio sounding when they occur. Fortunately, even during solar maximum, such bursts are sparse on time scales of an hour or more, and are therefore not considered a serious problem, although sounding data will be lost when they occur.

The AKR, which originates in the auroral zone at frequencies of 50-700 kHz, is often stronger in the region where a magnetospheric sounder must operate. Also, since it is related to the aurora, it tends to occur at interesting times for sounding. The AKR, on the other hand, is invariably discrete in frequency, sometimes having bandwidths as narrow as only 5 Hz [Gurnett and Anderson, 1981; Baumback and Calvert, 1987; Benson, et al., 1988]. Unpublished studies of the ISEE-1 and DE-1 high-resolution wave data also suggest that there are no detectable emissions between its discrete components [see Calvert, 1982]. It is thus feasible to eliminate AKR as broadcast stations are by modern digital sounders, by receiving first, then switching, if necessary, to an adjacent channel [Reinisch, 1986]. This technique is also easy to implement, and over the past decade has become a standard feature of modern digital ionosondes [Reinisch, et al., 1992]. Since this can be done quickly and there is plenty of room between the AKR discrete components (as shown in the figures of Gurnett and Anderson), this can also be accomplished without significantly affecting the quality of sounding. As a consequence, AKR can be eliminated by frequency side-stepping and therefore should not be a significant problem for radio sounding in the magnetosphere.

Terrestrial continuum is produced near the equator at the plasmapause and magnetopause, and tends to occur relatively often at flux levels ranging from 10^{-20} to 10^{-18} W/m^{2}Hz [Kurth, 1982; Gurnett, et al., 1988; R. R. Anderson, private communication, 1994]. It has also been found to consist of two components, as trapped continuum below the magnetopause plasma frequency in the distant tail, which is typically 30-40 kHz, and as escaping continuum above that frequency. Escaping continuum, despite its name, is also discrete [Kurth, et al., 1981] and can be eliminated by frequency side-stepping, as just described. Trapped continuum, on the other hand, results from the time average of many slowly-drifting components and is often too smooth in frequency to be eliminated by this method [see Kurth, et al., 1981, Figs. 1 and 2]. However, since by its nature it always occurs at frequencies below the maximum plasma frequencies of both the magnetopause and plasmapause, it should not significantly affect detecting these features or measuring plasma density in the plasmasphere.

4.2. Digital Integration

The key factor in radio sounding is detecting echoes with an adequate signal-to-noise ratio to measure echo directions, as discussed in Section 4.4. The signal-to-noise ratio (S/N) is the amplitude ratio of the received echoes to the pertinent noise threshold. The signal-to-noise ratio is therefore the square root of the power flux ratio between signal and noise in Figure 12. This signal-to-noise ratio, however, can be improved using pulse compression and spectral integration [Reinisch, 1986; Reinisch, et al., 1992], as follows.

4.2.1. Pulse Compression. Pulse compression involves transmitting a phase-modulated pulse consisting of n "chips" of length t, each chip being equivalent to a separate sounding pulse. The resulting echoes are then phase-correlated with the original modulation pattern to produce a composite echo which is the coherent sum of the n returning echo chips. The accompanying noise, on the other hand, adds incoherently, and therefore produces a composite noise signal which is only the square root of n times that of a single chip. Equivalent to adding n repeated measurements, this increases the signal-to-noise ratio by the square root of n, as illustrated in Figure 14. This figure shows the echo (B) of a 4-chip phase-coded pulse (A), consisting of four coherent echo signals of amplitude S accompanied by incoherent noise of amplitude N. The four echo chips are then phase shifted and added (C), producing a composite echo of amplitude nS accompanied by noise of amplitude $n^{1/2}N$. The resulting signal-to-noise ratio improvement is thus the square root of n (10 chips yielding a factor of $10^{1/2}$= 3.16, 100 chips yielding a factor of ten, etc.).

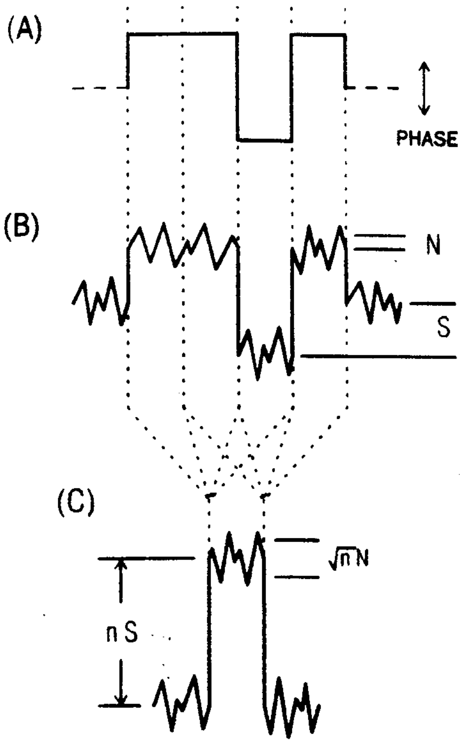

Fig. 14. Pulse compression, in which a phase-coded echo (B) is correlated with the original chip pattern (A) to improve the signal-to-noise ratio by the square root of n.

Using suitable modulation codes which suppress the contribution of adjacent echoes to the sum for a given echo delay, such pulse compression can be done for all overlapping sequences of n chips which have been received. It is thus possible to measure echoes delay in steps of a single chip, thereby improving the signal-to-noise ratio without sacrificing the spatial resolution. Its disadvantage, however, is that it requires transmitting a long, phased-coded pulse during which echoes cannot be received. For example, using a 53-millisecond coded pulse consisting of sixteen 3.3-msec chips would yield a factor-of-four signal-to-noise ratio improvement and 3.3 msec echo-delay resolution at the expense of being unable to receive echoes during the first 53 milliseconds of echo delay. Pulse compression thus increases the dead time before echoes can be received, in this case precluding the reception of echoes from any closer than about (53 msec)/(43 msec/R_E) = 1.2 R_E. Although this technique works best for echoes of long delay, like planetary radio echoes, it is still useful for magnetospheric sounding, using values for n of about 16 to 32, depending on the target distance.

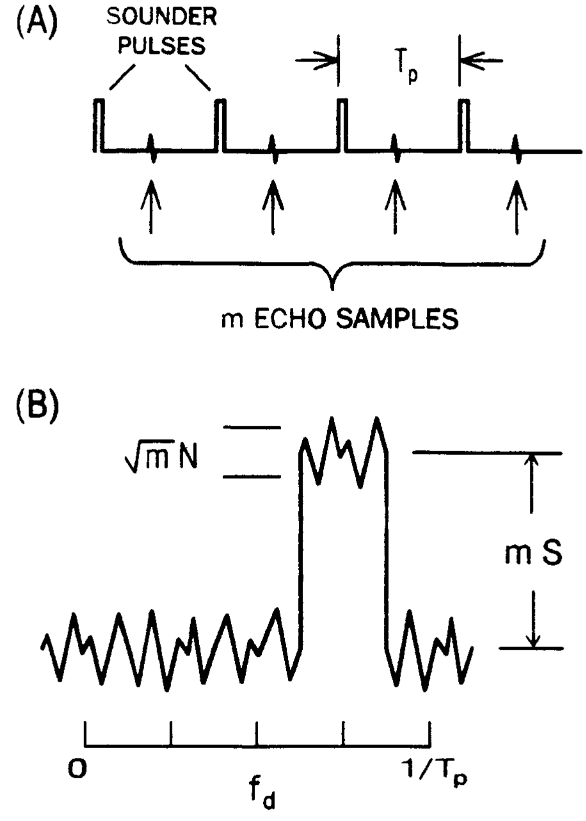

Fig. 15. Spectral integration, in which m echo samples for the same delay are spectrum analyzed to improve the signal-to-noise ratio by the square root of m.

4.2.2. Spectral Integration. Spectral integration, on the other hand, involves transmitting multiple pulses and spectrum-analyzing the echoes which are received at the same delays after each pulse (see Figure 15A). As with pulse compression, this yields a signal-to-noise ratio improvement equal to the number of pulses which are summed in the spectrum analysis. The basic concept is that spectrum analysis using m pulses is equivalent to averaging m repeated measurements of coherent echoes having a specific progressive phase shift between one pulse and the next. For echoes having a specific doppler shift or uniform phase shift caused by changing plasma conditions, all of the echo energy is deposited coherently into a single spectral channel, as shown in Figure 15B. Spectral integration thus produces m independent measurements consisting of the m possible echoes with different frequency offsets. The signal-to-noise ratio improvement for each of these echoes is then the square root of m, 100 yielding 20 dB, etc. The penalty of spectral integration, of course, is the additional time it take to transmit m pulses, and the trade-off thus becomes temporal resolution versus spatial resolution determined by the signal-to-noise ratio, as described in Section 4.4.

4.2.3. Doppler Measurement. An extra advantage of spectral integration is that it also yields the frequency spectrum produced by the doppler shift of satellite motion with respect to the sounding target. For a pulse repetition period T_p and m pulses, spectral integration yields m measurements of frequency shift over a frequency interval $1/T_p$ in steps of $1/mT_p$. For example, using $T_p = 0.5$ sec and $m = 8$, it would yield eight echo measurements over a 2 Hz interval in steps of 0.25 Hz. Doppler shifts from zero to 2 Hz would thus occupy the eight channels, and negative or larger doppler shifts, if they occur, would be aliased over this same 2 Hz interval. Since the velocity component v_d corresponding to a give doppler shift Δf_d, is given by

$$v_d = \frac{c}{2}\frac{\Delta f_d}{f} \tag{27}$$

this would be suitable for measuring velocity components of ±1.5 km/sec at 100 kHz, without aliasing and with about 400 m/sec velocity resolution. For a typical satellite velocity of 1.5 km/sec, this would permit distinguishing different echoes from eight different directions in equal cosine intervals from -180° to 180° with respect to the satellite velocity vector. The echo arrival direction can thus be determined to within about $\cos^{-1} 0.25 = 75°$ in the forward and backward directions, and to within about $\sin^{-1} 0.25 = 15°$ at right angles to these directions.

Although not useful for measuring echo direction, this is useful in two respects. First, it separates the echoes from different directions into separate spectral channels so their echo directions can be determined independently, as discussed in Section 4.4. This permits detecting multiple echoes from different directions at the same time, and this will be quite useful in distinguishing simultaneous echoes from the magnetopause and plasmasphere. Second, since the doppler measurement unambiguously determines the sense of the satellite velocity component in the echo direction, it can also be used to determine the hemisphere of echo arrival, and hence resolve the unavoidable 180° ambiguity of echo direction measurements from only the wave electric field. In other words, since it resolves this ambiguity, it permits absolute measurements of echo direction without magnetic antennas.

4.2.4. Combined Pulse Compression and Spectral Integration. Using both pulse compression and spectral integration yields an overall signal-to-noise ratio improvement equal to the square root of m times n:

$$S/N = \sqrt{m\,n}\; S/N_o \tag{28}$$

For example, using m = 8 and n = 16 would yield an overall signal-to-noise ratio improvement of $\sqrt{128} = 11.3$. This requires transmitting m phase-coded pulses of n chips each, followed by both lagged correlation and spectral analysis when the echoes are received. This, however, is easy to accomplish using modern digital computers, and the benefit, equivalent to having $11.3^2 = 128$ times more transmitter power, is worth the complexity it entails.

4.2.5. Typical Measurement. In order to clarify how measurements will be made, the following specific example will illustrate how the echo data will be recorded and analyzed. An echo measurement at a given frequency, using 8-point spectral integration, 16-chip pulse compression, a chip length of t = 3.3 msec, and a pulse repetition period of $T_p = 0.5$ seconds, requires transmitting eight 16 x 3.3 = 53-msec coded pulses in 4 seconds and sampling the echoes received at 3.3 msec intervals during each of the 500 - 53 = 457-msec periods between pulses.

This yields 457/3.3 = 135 echo samples per pulse, and 135 - 15 = 120 overlapping pulse-compression echo patterns for each pulse, since the last 15 echo patterns in the interval are incomplete. Pulse-compression thus yields 120 measurements of echo amplitude, corresponding to echo delays from 53 to 449 msec after each pulse (1.2 to 10.4 R_E). These echo signals for the eight pulses are then spectrum analyzed, eight at a time for the same equal delay after each pulse. This requires 120 eight-point FFT calculations for each of three antennas, or a total of 360 calculations. This then produces an array 3 x 120 x 8 = 2880 complex spectral amplitudes representing the echoes for 3 antennas at 120 delays with 8 spectral shifts. The echo directions are then computed for each delay and spectral shift, yielding 120 x 8 = 960 measurements of echo amplitude and direction. The result of a sounding measurement at a given frequency is thus nearly a thousand measurements of echo amplitude and direction, and this process is then repeated for the next frequency. The sounder, in this example, is thus capable of detecting up to 240 echoes per second having 120 different echo delays and 8 different doppler shifts.

Using modern microcomputers, these calculations require only a fraction of the four seconds allocated for the measurement, and can be carried out without delay while the next array of echo samples is being accumulated. The raw data rate, assuming eight-bit quantities are used for the resulting three quantities representing echo direction and amplitude, is 3 x 8 x 960 = 23,040 bits every four seconds, or 5760 bits/sec. Using standard data-compression techniques, these data can be compressed by a factor of five or more, so the nominal data rate of the instrument is roughly 1 kbit/sec.

4.3. Signal-to-Noise Ratio

The signal-to-noise ratios for the echo fluxes in Figure 12, before and after digital integration, are shown in Figure 16, for m = 8 and n = 16. For other integration parameters, these signal-to-noise ratios will increase or decrease by a factor of two for each combined factor of 4 for m and n; m = 4 and n = 8, for example, yielding half the indicated values, etc.

The expected post-integration signal-to-noise ratios are a hundred or more for the main magnetospheric sounding targets, and this will be used below to determine the spatial resolution. As discussed above, the sounder necessary to achieve this requires a 10-watt, 3000-volt transmitter, two 500-meter transmitting antennas, and a 10-meter spin-axis receiving antenna. Since the signal-to-noise ratio is proportional to the square root of the echo power flux, it increases proportional to the transmitter voltage below the breakpoint frequency in Equation 21 and as the square root of the power above that frequency. At low frequencies, below the breakpoint, it increases proportional to the square of the transmitter antenna length, according to Equation 21, and at frequencies below the noise-threshold crossover in Figure 12 it also increases proportional to the receiving antenna length. Although at high frequencies the only option for improving the signal-to-noise ratio is increasing the maximum transmitter power, at low frequencies it could be improved by increasing the root antenna voltage, antenna lengths, or both. These results pertain to a 300 Hz receiver bandwidth, and the signal-to-noise ratio is also inversely proportional to this bandwidth.

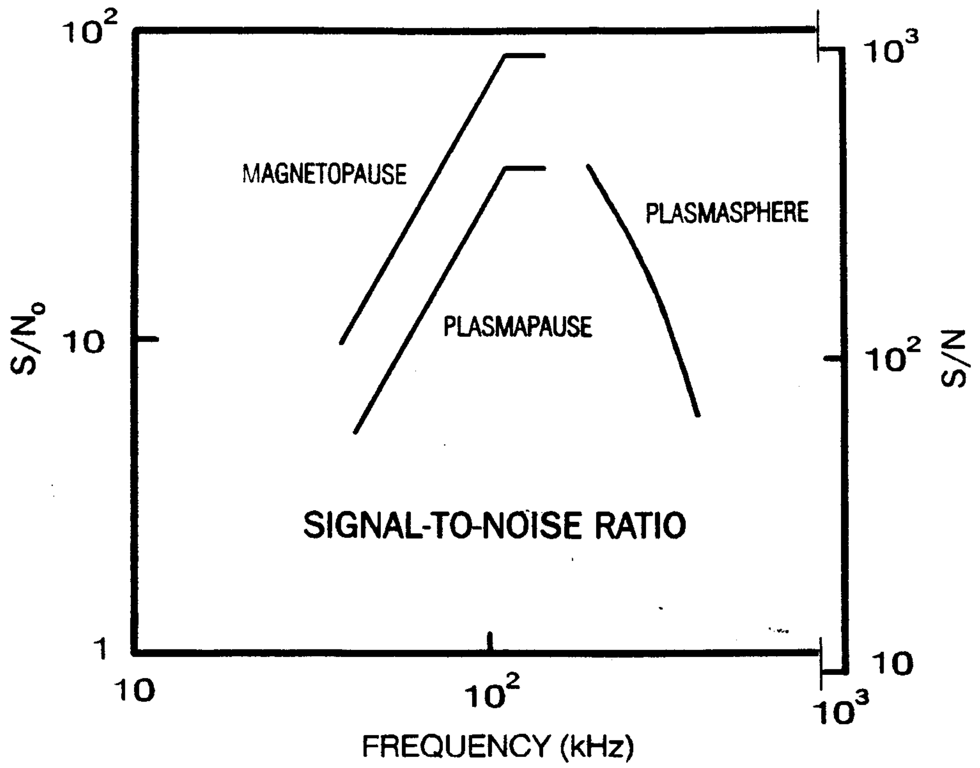

Fig. 16. Signal-to-noise ratio before (S/N_o) and after (S/N) sixteen-chip pulse compression and eight-point spectral integration.

4.4. Direction Measurement

Although in the ionosphere echo paths are generally vertical because of horizontal stratification, in the magnetosphere where echoes may arrive from any direction, it is necessary to measure their direction. Since these directions are approximately perpendicular to the so-called *E-plane* of the wave [see Allis, et al., 1963, Ch. 4], as shown in Figure 17, it is sufficient to measure these directions from three orthogonal components of the wave electric field. This requires coherent reception using three orthogonal dipole antennas, as shown in Figure 2, and this yields three pairs of in-phase and quadrature echo signals representing the electric-field amplitude and phase in three orthogonal directions. The echo direction can then be determined from the vector cross-product of corresponding in-phase and quadrature values, represented by E and E' in Figure 17, since this yields three quantities proportional to the wave amplitude and direction cosines of the E-plane normal.

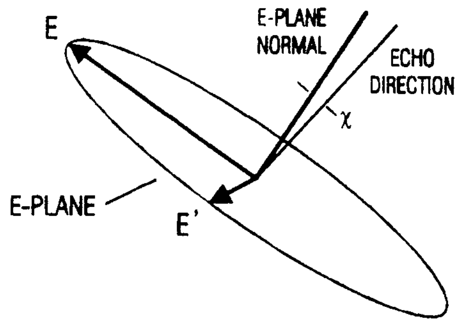

Fig. 17. E-plane normal determined by the inphase and quadrature electric field vectors E and E', where χ (usually small) is the wave-normal deviation angle

Calculating echo directions thus requires a straightforward vector cross product of six signals measured by three radio receivers, and it is best to do this on-orbit to conserve telemetry bandwidth. It is also stressed that the three antennas and phase-coherent radio receivers are not a luxury for a magnetospheric sounder, since all three are needed to measure echo directions.

Except near a cutoff for waves almost exactly perpendicular to the magnetic field, the E-plane normal represents an adequate approximation for the echo direction. Under certain circumstances, however, it will be necessary to correct for the wave-angle tilt χ of the E-plane normal with respect to the wave normal, as discussed by Allis, et al. [1963] and shown in Figure 17. In addition, it will also sometimes be necessary to correct for the difference between the wave-normal and ray-path directions, since it is the latter which actually determines the echo direction, and these can sometimes be significantly different [see Calvert, 1966]. These corrections, however, are well understood and can be determined from the local density, magnetic field, and wave mode determined by the sounder. The resulting ray directions must then be analyzed by ray-tracing and echo-distance inversion techniques which are well developed for the ionosphere and other applications [see Jackson, 1969a; 1969b], but remain to be adapted for the magnetosphere. Also, since the wave electric field is the same for opposite propagation directions [see Allis, et al., 1963], this leaves undetermined the sense of propagation along the echo direction, and it is necessary to resolve this directional ambiguity as described above, or from systematic changes of echo direction with orbital position.

5. PRECISION AND RESOLUTION

The precision of a sounder is dictated by the spatial, temporal, and density resolution it can achieve, and it will be shown that these depend mostly on the signal-to-noise ratio. Other factors, like the absolute precision of its density and distance measurements, are determined by frequencies and times which can easily be measured to high precision with standard electronics. A sounder is thus automatically an absolute instrument, and precise calibration is not required. Also, by measuring the plasma

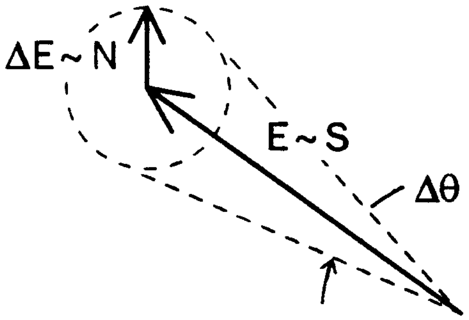

Fig. 18. Angular uncertainty Δθ of electric-field measurement for a signal S and random noise signal N.

frequency remotely with waves, it measures the most fundamental wave property of a plasma without affecting the plasma being measured. As a consequence, except as discussed below, the only significant source of measurement error involves the ray-tracing and echo-distance inversion techniques mentioned above. Analyzing these errors, however, is beyond the scope of this study, and will be addressed separately.

5.1. Angular Precision and Spatial Resolution

5.1.1. Angular Precision. As shown in Figure 18, the electric vectors E which are used to determine the echo direction will be accompanied by a vector noise signal ΔE, equal in magnitude to the electric field divided by the signal-to-noise ratio. This introduces an angular uncertainty of ±ΔE/E in the electric field direction, and hence also in the echo directions determined from E. The angular precision Δθ of a sounder thus equals twice the reciprocal signal-to-noise ratio:

$$\Delta\theta = 2\,\frac{\Delta E}{E} = \frac{2}{S/N} \qquad (29)$$

A signal-to-noise ratio of 100 thus corresponding to a full-width angular precision of 0.02 radians, or about one degree.

5.1.2. Spatial Resolution. As shown in Figure 19, the transverse spatial resolution Δs = s Δθ, at a distance s, is

$$\Delta s_{\perp} = s\,\Delta\theta = \frac{2\,s}{S/N} \qquad (30)$$

The transverse resolution for a signal-to-noise ratio of 100 is thus about 500 km at a distance of four earth radii. The range resolution, on the other hand, is determined by the chip length t and speed of light c:

$$\Delta s_{\parallel} = \frac{c\,t}{2} = \frac{c/2}{\Delta f_t} \qquad (31)$$

where c/2 = 150 km/msec and Δf_t = 1/t is the bandwidth corresponding to the chip length t. A chip length of 3.3 msec thus yields 500 km range resolution.

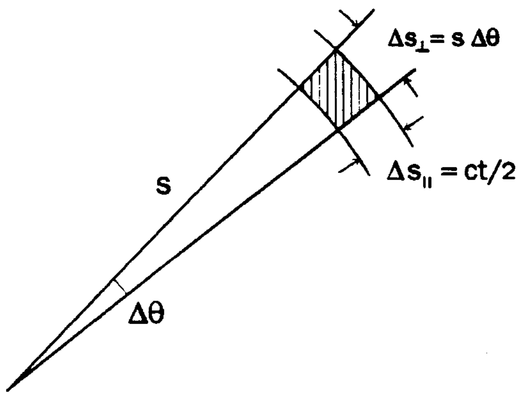

Fig. 19. Transverse resolution $\Delta s_{\perp}$ determined by the distance s and angular resolution Δθ, and the range resolution $\Delta s_{\parallel}$ determined by the chip length t.

The optimum bandwidth for receiving chips of length t is Δf = 1/t = Δf_t, since a wider bandwidth introduces unnecessary noise and a narrower bandwidth cannot pass the necessary frequency components of the echo waveform. The optimum bandwidth for t = 3.3 msec is 300 Hz, as assumed for Figures 12 and 16. The sounder configuration introduced above is thus optimum for 1° angular resolution and 500 km spatial resolution in all three directions at 4 R_E over the frequency range from of 30 to 300 kHz in Figure 16 where the signal-to-noise ratio exceeds 100.

5.1.3. Bandwidth Selection. If the receiver bandwidth is varied, the noise power within this bandwidth increases proportional to the bandwidth. As a consequence, according to equation 30, the transverse spatial resolution is proportional to the square root of the bandwidth:

$$\Delta s_{\perp} \sim \sqrt{\Delta f} \tag{32}$$

On the other hand, if the chip length is varied, the range resolution is proportional to chip length, and hence inversely proportional to the chip bandwidth:

$$\Delta s_{\parallel} \sim 1 / \Delta f_t \tag{33}$$

Consequently, if both are varied and an optimum bandwidth ($\Delta f = \Delta f_t$) is maintained,

$$\Delta s_{\parallel} \, \Delta s_{\perp}^2 = \mathit{constant} \tag{34}$$

and the total volume resolution remains the same.

This result will be useful in selecting the best bandwidth and chip length for a given sounder measurement. For example, if the magnetopause distance is more important than its transverse structure, one might use a pulse length of 3.3/5 = 0.66 msec and a bandwidth of 1500 Hz, for a range resolution to 100 km. Equation 34 would then imply that the transverse resolution would then increase by the square root of five, to become 1100 km.

5.2. Density Resolution

The intrinsic density resolution of a sounder also depends on the bandwidth, according to Equation 1:

$$\frac{\Delta N_e}{N_e} = 2 \frac{\Delta f}{f} \tag{35}$$

The intrinsic resolution for a bandwidth of 300 Hz therefore varies from about 2% at 30 kHz to 0.2% at 300 kHz.

The actual density resolution, on the other hand, is usually determined by the frequency step between adjacent sounding frequencies. According to Equation 35, for example, a density resolution of 10% would require 5% frequency resolution, and hence $1/\log_{10}(1.05)$ = 47 logarithmic frequency steps per decade.

5.3. Temporal Resolution

The total time t_{total} for a complete measurement equals the number of frequencies times m times the pulse repetition period T_p. For a logarithmic frequency sweep with constant fractional density resolution:

$$t_{total} = m\ T_p\ \frac{\log_{10}(f_2/f_1)}{\log_{10}(1 + \Delta f/f)} \tag{36}$$

where f_1 and f_2 are the lower and upper frequency limits. The time required for sounding between 30 and 300 kHz with 10% density resolution, using m = 8 and T_p = 0.5 sec, is therefore 8 x 0.5 x 1 x 47 = 188 seconds or about 3 minutes. This then becomes the temporal resolution for measuring the magnetopause, plasmapause, and plasmasphere with 500-km spatial resolution in three dimensions and 10% density resolution.

6. CONCLUSIONS

This paper has demonstrated the feasibility of radio sounding in the magnetosphere and discussed the major factors affecting the design of a practical sounder. A suitable sounder would use three-axis dipole antennas to measure echo direction and be capable of measuring the density, distance, and direction of the magnetopause, plasmapause, and plasmasphere from 30 to 300 kHz, with 10% density resolution and 500-km spatial resolution, in about three minutes.

The critical factors affecting sounder performance are the antenna lengths and the transmitter voltage at the root of the transmitting antennas. Using 500-meter transmitting antennas and a 3-kV, 10-watt transmitter, it is feasible to detect echoes at distances of four Earth radii with 1° angular resolution.

Using pulse compression and spectral integration, it is feasible to detect echoes at 30-300 kHz with signal-to-noise ratios of a hundred or more, and it has been show that the angular precision, in radians, equals twice the reciprocal signal-to-noise ratio. It has also been shown that volume resolution of a sounder is constant when the chip length and bandwidth are varied.

Multiple echoes, distinguishable by their different delays and doppler shifts, should be detected from the magnetopause, and as a result it should be possible to measure the distance and approximate shape of the magnetopause in a matter of seconds. The predicted strength of echoes from the plasmapause has also been analyzed as a function of latitude, and it has been found that multiple, focused echoes should occur in the polar region. A new formula has also been derived for specular reflection from curved surfaces, and the predicted focusing and defocusing by the magnetopause and plasmapause, by factors of 2 to 4, have been included in the analysis.

Acknowledgements. This paper is based on the pioneering work of Colin Franklin and John Jackson during the Alouette/ISIS Topside-Sounder Program, and is dedicated to the memory of Dave Florida and John Chapman. The authors also acknowledge useful suggestions by the Inner Magnetosphere Imager (IMI) Study Team headed by Tom Armstrong. This work was supported in part at the University of Iowa by NASA Grants NAG5-1926 and NAG8-1030, and at Nichols Research Corporation by NASA Contracts S07854-F and S22835-2.

REFERENCES

Allis, W. P., S. J. Buchsbaum, and A. Bers, *Waves in Anisotropic Plasmas*, MIT Press, Cambridge, Mass., 1963.

Appleton, E. V., Wireless studies of the ionosphere, *J. Inst. Elect. Eng.*, *71*, 642-650, 1932.

Baumback, M. M., and W. Calvert, The minimum bandwidths of auroral kilometric radiation, *Geophys. Res. Lett.*, *14*, 119-122, 1987.

Bennett, W. R., *Electrical Noise*, McGraw-Hill, New York, 1960.

Benson, R. F., M. M. Mellott, R. L. Huff, and D. A. Gurnett, Ordinary mode auroral kilometric radiation fine structure observed by DE-1, *J. Geophys. Res.*, *93*, 7515-7520, 1988.

Briet, G., and M. A. Tuve, A test for the existence of the conducting layer, *Phys. Rev.*, *28*, 554-575, 1928.

Bougeret, J. L., J. Fainberg, and R. G. Stone, Interplanetary radio storms, *Astron. Astrophys.*, *136*, 255-262, 1984.

Budden, K. G., *The Propagation of Radio Waves*, Cambridge Univ. Press, New York, 1985.

Calvert, W., Oblique Z-mode echoes in the topside ionosphere, *J. Geophys. Res.*, *71*, 5579-5583, 1966.

Calvert, W., and C. W. Schmidt, Spread-F observations by the Alouette topside sounder satellite, *J. Geophys. Res.*, *69*, 1839-1852, 1964.

Calvert, W., J. R. McAfee, R. B. Norton, T. L. Thompson, J. M. Warnock, and E. C. Whipple, A plasmapause sounder satellite, *NOAA Tech. Report ERL 242-AL-8*, 1972.

Calvert, W., The auroral plasma cavity, *Geophys. Res. Lett.*, *8*, 919-921, 1981a.

Calvert, W., The detectability of ducted echoes in the magnetosphere, *J. Geophys. Res.*, *86*, 1609-1612, 1981b.

Calvert, W., A feedback model for the source of auroral kilometric radiation, *J. Geophys. Res.*, *87*, 8199-8214, 1982.

Carpenter, D. L., and R. R. Anderson, An ISEE/whistler model of equatorial electron density in the magnetosphere, *J. Geophys. Res.*, *97*, 1097, 1992.

Carpenter, D. L., B. L. Giles, C. R. Chappell, P. M. E. Décréau, A. M. Persoon, A. J. Smith, Y. Corcuff, and P. Canu, Plasmasphere dynamics in the duskside bulge region: A new look at an old topic, *J. Geophys. Res.*, *98*, 19,243-19,271, 1993.

Davies, K., *Ionospheric Radio*, Peter Peregrinus Ltd., Short Run Press, Exeter, 1990.

Franklin, C. A., and M. A. Maclean, The design of swept-frequency topside sounders, *Proc. IEEE*, *57*, 897-929, 1969.

Green, J. L., R. F. Benson, D. Carpenter, W. Calvert, S. F. Fung, D. Gallagher, P. H., Reiff, B. W. Reinisch, M. F. Smith, and W. W. L. Taylor, Radio imaging for the proposed Magnetospheric Imager (IMI) mission (report), submitted to IMI Committee, 35 pp., 1993.

Green, J. L., and S. F. Fung, Radio sounding of the magnetosphere from a lunar-based VLF array, accepted for publication in *Adv. in Space Research*, 1993.

Gurnett, D. A., and R. R. Anderson, The kilometric radio emission spectrum: Relationship to auroral acceleration processes, in *Physics of Auroral Arc Formation*, Geophys. Monogr. Series 25, Akasofu and Kan, eds., AGU, 341-350, 1981.

Gurnett, D. A., W. Calvert, R. L. Huff, D. Jones, and M. Sugiura, The polarization of escaping continuum radiation, *J. Geophys. Res.*, *93*, 12,817-12,825, 1988.

Jackson, J. E, Reduction of topside ionograms to electron-density profiles, *Proc. IEEE*, *57*, 960-975, 1969a.

Jackson, J. E, Comparison between topside and ground-based soundings, *Proc. IEEE*, *57*, 976-985, 1969b.

Jordan, E. C., *Electromagnetic Waves and Radiating Systems*, Prentice-Hall, Englewood Cliffs, N. J., 1950 (Subsequently revised by Jordan and Balmain.).

Kurth, W. S., D. A. Gurnett, and R. R. Anderson, Escaping nonthermal continuum radiation, *J. Geophys. Res.*, *86*, 5519-5531, 1981.

Kurth, W. S., Detailed observations of the source of terrestrial narrowband electromagnetic radiation, *Geophys. Res. Lett*, *9*, 1341-1344, 1982.

Ratcliffe, J. A., The magnetoionic theory, *Wireless Engineer*, *10*, 354-363, 1933.

Ratcliffe, J. A., *The Magnetoionic Theory and its Application to the Ionosphere*, Cambridge Univ. Press, Cambridge, 1959.

Reiff, P. H., J. L. Green, R. F. Benson, D. Carpenter, W. Calvert, S. F. Fung, D. Gallagher, B. W. Reinisch, M. F. Smith, and W. W. L. Taylor, Radio imaging of the magnetosphere, *EOS Trans. AGU*, *75*, 129-134, 1994

Reinisch, B. W., New techniques in ground-based ionospheric sounding and studies, *Radio Sci.*, *21*, 331-341, 1986.

Reinisch, B. W., D. M. Haines, and W. S. Kuklinski, The new portable Digisonde for vertical and oblique sounding, NATO-AGARD Conference Proceedings, AGARD-CP-502, Feb. 1992.

Schmerling, E. R., and R. C. Langille, Introduction (1969 Special Issue on Topside Sounding), *Proc. IEEE*, *57*, 859-860, 1969.

Stix, T. H., *The Theory of Plasma Waves*, McGraw-Hill, New York, 1962.